# Local and remote influences on the heat content of Southern Ocean mode water formation regions.

**Emma J. D. Boland[1], Daniel C. Jones[1], Andrew J. S. Meijers[1], Gael Forget[2], and Simon A. Josey[3].**

[1]British Antarctic Survey, High Cross, Madingley Road, Cambridge, United Kingdom
[2]Massachusetts Institute of Technology, Cambridge, MA, USA
[3]National Oceanography Centre, European Way, Southampton, United Kingdom

**Key Points:**

- The heat content of Southern Ocean mode waters is sensitive to heat flux and wind stress changes.
- Sensitivities are highest to local recent heat flux, and non-local past year wind stress changes.
- High sensitivity regions reveal source waters and dynamic links with boundary current regions.

Corresponding author: Emma J. D. Boland, `emmomp@bas.ac.uk`

## Abstract

The Southern Ocean (SO) is a crucial region for the global ocean uptake of heat and carbon. There are large uncertainties in the observations of fluxes of heat and carbon between the atmosphere and the ocean mixed layer, which leads to large uncertainties in the amount entering into the global overturning circulation. In order to better understand where and when fluxes of heat and momentum have the largest impact on near-surface heat content, we use an adjoint model to calculate the linear sensitivities of heat content in SO mode water formation regions to surface fluxes. We find that the heat content of these regions is, in all three basins, most sensitive to recent, local heat fluxes, and to non-local wind one to eight years previously. This is supported by the calculation of sensitivities to potential temperature changes at constant density, which reveal the sources of the mode water formation regions, and by sensitivities to potential temperature changes with varying density, which reveal dynamic links with boundary current regions, the Antarctic Circumpolar Current, and wave-like features. A series of forward perturbation experiments in the fully non-linear model confirm that the adjoint model can accurately predict linear changes in heat content of fixed volume mode water formation regions. These experiments also highlight that nonlinear effects can be of importance, depending on the time and region investigated, and that the contribution of volume changes to heat content changes can be as large as or larger than the contribution from temperature changes.

Plain Language Summary: The Southern Ocean is of crucial importance to the global ocean's uptake of carbon and heat. However, due to difficulties in making observations in such a remote and hostile environment, we currently don't know accurately how much heat and carbon enters the Southern Ocean from the atmosphere. Heat from the Southern Ocean can get locked away for hundreds to thousands of years in the world's deep oceans, entering through a few key regions. We use a computer model to assess how the heat, fresh water, and wind energy entering through the surface of the Southern Ocean affects the heat of these key regions. We find that these regions are very sensitive to heat coming in through the surface directly over them, and that winds across a wider area of the Southern Ocean can affect the heat stored for several years. If we want to estimate the heat stored in these regions more accurately, this information can be used to help us decide where and when it is important to measure the winds and heat entering the ocean better.


## 1 Background

The Southern Ocean (SO) is home to the world's longest and strongest ocean current, the Antarctic Circumpolar Current (ACC), which encircles the globe free of continental barriers. Driven by strong wind and buoyancy forcing, the ACC transports climatically important tracers such as heat, salinity, and carbon between the three major ocean basins. These forcings also create sloping density surfaces (isopycnals) which tilt upwards from north to south, which connect deep waters from around the globe to the surface. At the surface, air-sea interactions modify the properties of water masses. These modified waters then return to depth and into the other ocean basins as dense waters near the Antarctic continental shelf, or as lighter mode and intermediate waters north of the ACC (Lumpkin & Speer, 2007; Marshall & Speer, 2012).

The Southern Ocean is of critical importance to the global oceanic uptake of heat and carbon, due in part to this overturning circulation. It may be responsible for as much as 75% of the global ocean heat uptake and approximately 50% of the carbon uptake (Frölicher et al., 2015; Mikaloff Fletcher et al., 2006). Roughly 30% of anthropogenic $CO_2$ emissions ends up in the ocean (Khatiwala et al., 2013), and over 93% of this excess heat has been estimated to be stored in the ocean (Levitus et al., 2012), predominantly in the SO (Roemmich et al., 2015).

Understanding what determines the time scales of Southern Ocean overturning and the properties of the waters transported is of crucial importance to future climate predictions, including the continued efficiency of the carbon sink (Landschützer et al., 2015; Le Quéré et al., 2018). The properties of the overturning circulation are affected by a range of processes, including variations in surface forcings, variations in the interactions of these forcings with ocean mixed layer properties, and variations in the draw-down of mixed layer properties into the ocean interior as mode, intermediate, and deep waters. Unfortunately, direct air-sea flux observations are scarce in the Southern Ocean, especially in the winter when sea ice hinders access to the region (Newman et al., 2015). This work focuses on understanding how variations in surface forcings impacts on mode water formation regions within the mixed layer, using a data-constrained estimate of these processes instead (ECCOv4, Forget, Campin, et al., 2015). This will provide insights into the influence of uncertainties in observations of surface forcings on estimates of mode water properties, as well as for estimating the impact of future changes in these forcings.

For this study, we use an adjoint model to assess the impact of surface forcings on the heat content of mode water formation regions (MWFRs). Adjoint models calculate linear sensitivities to quantities of interest known as 'objective functions', see section 2 for further details. Using the adjoint approach, one does not have to theorize what variable is the most relevant for setting your quantity of interest, as the sensitivities are calculated at all points in the model domain at multiple time lags for all state variables. However, because the adjoint model is linear, it does not replace the need for full, non-linear simulations, as there are important processes that will not be fully captured in adjoint sensitivity fields. Adjoint models are thus best suited to looking at quantities one can expect to be largely controlled by linear effects over relatively large volumes and time periods. In this context, a linear effect might be the advection of a passive tracer, and a non-linear effect might be convective mixing, and in this work, we investigate basin-scale averages over 3 months. The suitability of the linear approximation for these scales is confirmed in section 4 – we expect the response to become less linear at more local and/or shorter timescales. For a more thorough discussion of adjoint models, including the setup used in this study, refer to section 2 in Jones et al. (2018) and references therein.

## 2 Experiment Design

For this study we used the ECCOv4 (release 2) ocean state estimate framework (Forget, Campin, et al., 2015). This is a global $\sim 1°$ ocean and sea ice setup of the MITgcm model (Adcroft, Campin, Hill, & Marshall, 2004) that spans 20 years from 1992 to 2011, with surface forcings and initial conditions that have been optimized to reduce misfits to observations. Details of the 4D-Var optimization process and the residual model-data misfit can be found in Forget, Campin, et al. (2015). We chose to use this set-up as it not only provides a recent, well-constrained estimate of the Southern Ocean, but also because it can be easily modified to carry out adjoint sensitivity experiments, in which we examine the linear sensitivity of a quantity of interest to a set of model state variables and surface forcings.

Our study is dependent in particular on the mixed layer depths in ECCOv4 to define mode water formation regions, and these closely match observations in terms of geography and magnitude (see figure 6, Forget, Ferreira, & Liang, 2015). Figure S1 in the supplementary information of Jones et al. (2019) shows a comparison of the sea level anomaly and sea surface temperatures in ECCOv4 with observations in the Indian and Pacific mixed layer regions also used in this study, showing that absolute values and variability are well captured. Figure 1 compares the salinity and temperature in the Pacific Mode Water Formation Region, as defined below. The equivalent plots for the Atlantic and Indian basins are included in the supplementary information, see figures S1,2.

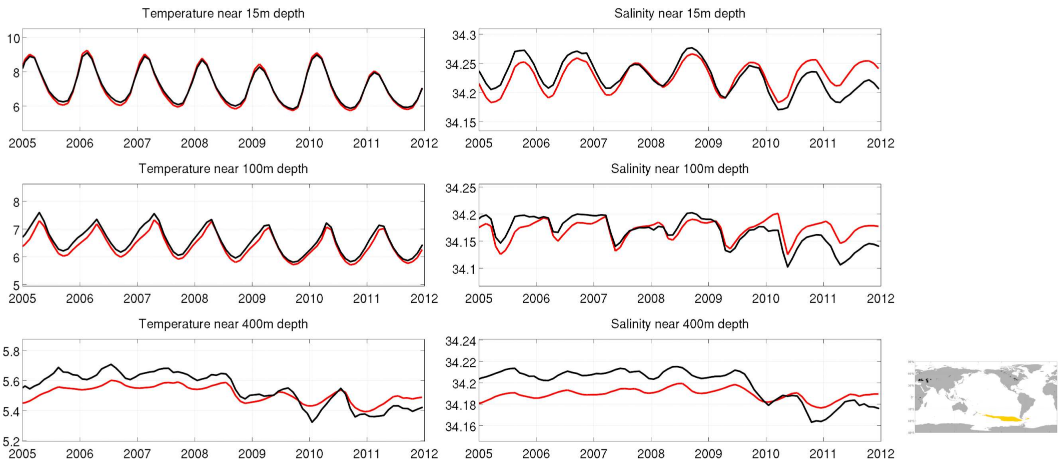


**Figure 1.** Comparison of direct measurements from ARGO floats (black line, see `www.argo.ucsd.edu` for more info) and the ECCOv4r2 solution, sub-sampled identically (red lines) with, for potential temperature (left) and salinity (right), in the median Pacific mode water formation region (yellow-shaded area bottom right, see text for how this region is defined). The ARGO dataset of profiles is interpolated to standard depths, and then the ECCO model is sub-sampled identically to produce comparative profiles. The black line is the sum of the 3 month running mean of the ECCO profiles at that depth (red line) and the median ARGO-ECCO profile misfit.

An adjoint model, in this context, is one that starts from a quantity of interest (henceforth referred to as an 'objective function'), such as the integrated temperature or salinity over a certain region, and steps backwards through a linearized version of the model, propagating the sensitivities of the objective function. This process is directly tied to the state of the forward non-linear model run. The adjoint model produces the linear sensitivity of the objective function to a range of specified model variables, such as surface fluxes or interior properties (e.g. potential temperature, mixing parameters). The objective function can be an arbitrary function of the model state, but is often a quantity of interest in a defined volume integrated over a specific time period in the full non-linear model. In a more traditional model study, one might start by choosing a model variable or variables theorized to impact one's quantity of interest, and then carry out a suite of perturbation experiments changing these variables by a range of magnitudes, locations, and/or times. By comparison with a control run, one then infers the sensitivity of the quantity of interest to the perturbation points in the model, simulation by simulation. In contrast, an adjoint model can produce in one single model run the linear sensitivity of one's quantity of interest to a range of model variables, at all points in the model domain, at multiple time lags.

For this study, our quantity of interest was the heat content of SO mode water formation regions. By definition, such water is characterized by low stratification (i.e. low potential vorticity (PV) values) (see e.g. Hanawa & Talley, 2001). Figure 2 shows a latitude-depth plot along 90°E (in the Indian sector of the Southern Ocean) of the minimum PV values for a representative year (1999) from the ECCOv4 r2 state estimate (notice the logarithmic color scale). There is a sharp lateral gradient in the minimum PV values just inside the winter mixed layer extent, and as such the winter mixed layer extent captures the mode water formation pools of interest.

Three distinct mode water formation pools can be identified in the three main basins - Atlantic, Pacific, and Indian (figure 3a). The winter mixed layer encloses the mode wa-

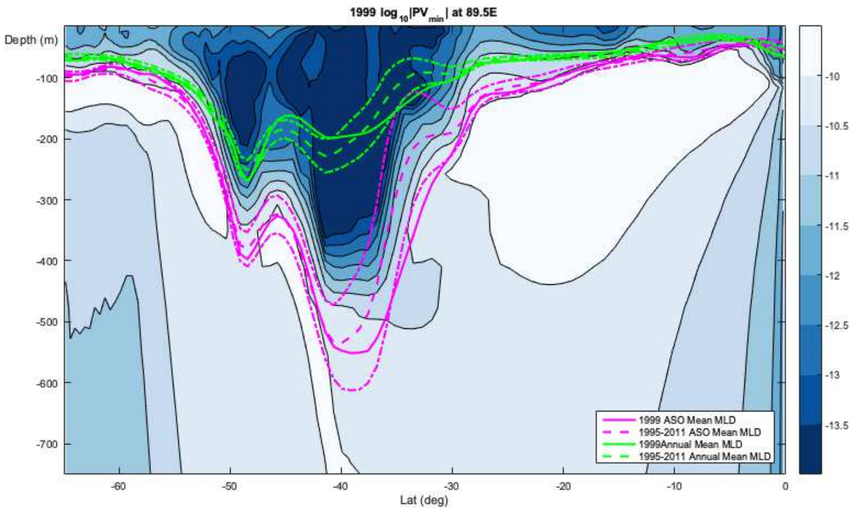


**Figure 2.** An example mode water formation region, characterized by low PV values, contained within the winter mixed layer: Latitude-depth plot of the absolute value of the 1999 minimum PV along 90°E in ECCOv4 r2, on a log scale (color). Also shown are the August-October (ASO) mean mixed-layer depth for 1999 (pink line) and 1995-2011 mean and standard deviations (pink dashed and dash-dotted lines) and the annual mean mixed-layer depth (MLD) for 1999 (green line) and 1995-2011 mean and standard deviations (green dashed and dash-dotted lines).

ter formation pools (see also figure 2). We used a combination of annual minimum PV values and winter (ASO) mixed layer depths to form the horizontal mask for the 'objective function' volume for the suite of adjoint experiments we carried out, whilst ensuring that nothing too close to land or too far north was included. Specifically, we defined the objective function as anywhere between 30 and 65°S with a minimum PV value of less than $10^{-13}$ and an ASO mean mixed-layer depth (MLD) (for that given year) of greater than 300m depth, then manually removed regions in the North of the basins[1], as we wished to concentrate on the main mode water pools. This mask as calculated for 1999 is shown by the black dotted line in figure 3a. The objective function regions are referred to throughout as MWFRs (mode water formation regions).

The climatology of the heat content of the volume of mode water (defined horizontally via the mask and integrated to the depth of the instantaneous mixed layer) for each of the three basins can be seen in figure A.1. The Indian pool has the largest heat content, followed by the Pacific and Atlantic pools. All three peak in September with a minimum in January or February.

We split the Southern Ocean into three basins using the three latitudinal black dashed lines shown in figure 3a, and calculate a separate objective function for each basin. The Indian and Pacific basins are divided at 180°W, the Pacific and Atlantic at 49.5°W and the Atlantic and Indian at 30.5°E. Because the adjoint model calculates linear sensitivities, the total Southern Ocean sensitivity to a given model variable will be the sum of the sensitivities for each basin, i.e.

$$J^Y_{\mathrm{SO}} = J^Y_{\mathrm{Atl}} + J^Y_{\mathrm{Pac}} + J^Y_{\mathrm{Ind}}, \tag{1}$$

[1] We removed regions north of 40°S in the Pacific and East Indian Ocean (60°W to 110°E), north of 35°S in the West Indian Ocean (110°E to 60°E) and north of 45°S close to South America (49.5°W to 75°W).

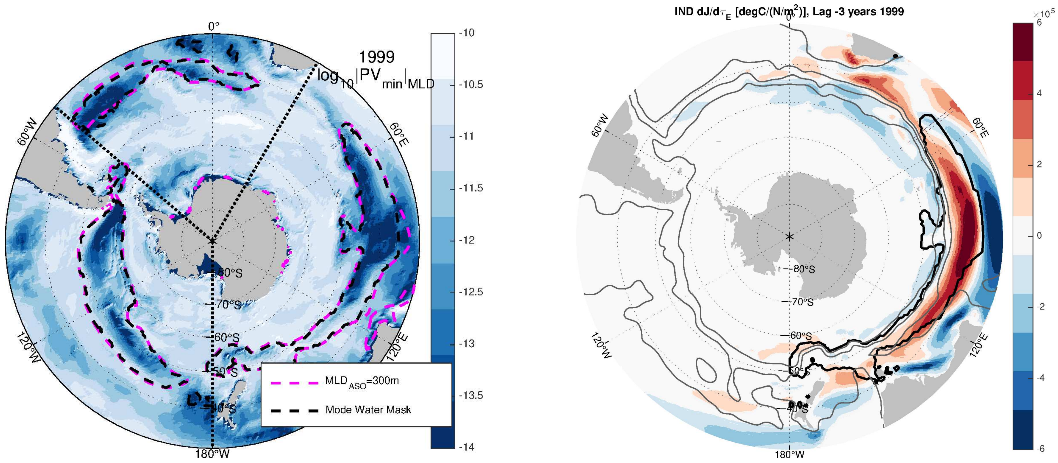


**Figure 3.** a) The winter mixed layer encloses mode water formation pools laterally: Blue colors are the absolute value (on a $\log_{10}$ scale) of the 1999 minimum PV at the annual mean mixed-layer depth (the green dash-dotted line in figure 2). Also shown are the 300m August-October mean mixed-layer depth contour (pink dotted line) and the extent of the mode water mask (black dashed line), as described further in the text. The domain is also divided into three basins by the three longitudinal black dotted lines shown, into the Atlantic, Indian, and Pacific basins referenced throughout. b) An example sensitivity field: Colors indicate the adjoint sensitivity of the 1999 Indian MWFR heat content to zonal wind stress at approx. 3 years lag. The grey contours indicate the -17, 0, and 30 Sv mean barotropic streamlines, for the entirety of ECCOv4 r2, chosen to highlight the boundary between of the ACC and the sub-tropical gyre structure.

where $J_b^Y$ is the objective function in the given basin $b$ in year $Y$, and thus

$$\frac{\partial J_{\text{SO}}^Y}{\partial X}(\underline{r}, t) = \frac{\partial J_{\text{Atl}}^Y}{\partial X} + \frac{\partial J_{\text{Pac}}^Y}{\partial X} + \frac{\partial J_{\text{Ind}}^Y}{\partial X}, \tag{2}$$

where $\partial J_b^Y / \partial X(\underline{r}, t)$ is the linear adjoint sensitivity of the objective function $J_b^Y$ to model variable $X$ at point $\underline{r} = (x, y, z)$ and time $t$.

We re-calculated the objective function based on the same MLD and minimum PV criteria for each of the 20 years in ECCOv4 r2. We chose the annual maximum winter mixed layer depth as the vertical extent of our objective function [denoted $\max(\text{MLD}_{\text{ASO}})$]. To capture the peak of mode water formation, we chose our objective function to extend to the two months on either side of the peak heat contents of the three basin volumes, i.e. from July to November (see figure A.1). Thus, our full objective function for a given year and basin is defined as the following volume averaged heat content:

$$J_b^Y = \frac{1}{V_b^Y \Delta t} \int_{\text{Jul}}^{\text{Nov}} \iint^{f_b(x,y)} \int_{z=0}^{\max(\text{MLD}_{\text{ASO}})} \rho_0 \, c_p \, \theta(\text{r}, t) \, dt \, dxdy \, dz, \tag{3}$$

where $V_b^Y = \iint^{f_b(x,y)} \int_0^{\max(\text{MLD}_{\text{ASO}})} dxdy \, dz$ is the control volume in year $Y$ and basin $b$, $\Delta t$ is the averaging time interval, $f_b(x, y)$ is the horizontal mask in basin $b$; $\rho_0$, a reference density; $c_p$, the heat capacity of sea water; and $\theta$, the potential temperature. Note that the extent of the objective function region is calculated offline and so is a fixed volume. The effect of choosing our objective function as defined above, with the lateral extent limited using our mask, rather than just looking at the entire Southern Ocean mixed layer, is briefly investigated in section A.2.

In order to better understand inter-annual variability and have better statistical behavior, we carried out an ensemble of adjoint runs, each with objective functions defined in different years. After a number of test runs, we determined that the majority of sensitivity magnitudes had decayed significantly by around 8 years prior to the start of the objective function. Thus we settled on an ensemble of 13 eight-year adjoint runs, with objective functions defined in each winter from 1999 to 2011.

An example sensitivity field, the sensitivity of the 1999 Indian MWFR heat content to zonal wind stress at approximately 3 years lag, can be seen in figure 3b. Thus, red (blue) colors indicate where an increase (decrease) in zonal wind stress in 1996 would result in an increase in the Indian MWFR heat content in 1999. The sensitivity has been scaled by $1/\rho_0 c_p$, and thus units indicate the number of degrees C the similarly scaled MWFR heat content would rise if the zonal wind stress changed by 1 N/m$^2$.

# 3 Adjoint Results

## 3.1 Sensitivities to Surface Properties

A range of example ensemble mean sensitivities of the MWFRs to various surface properties can be seen in figure 4, chosen to highlight the range of and main properties of our results. For each ensemble member, sensitivities were output at two week intervals as averages over those two weeks. The sensitivities shown in figure 4 are ensemble averages of winter (July to September) averages, which are then multiplied by a representative scalar standard deviation for the surface property $\sigma_0$ (these values can be found in table 1) and scaled by $1/\rho_0 c_p$. This makes the units of sensitivity the amount by which a unit perturbation of the given surface property at the relevant point in space and time would raise the objective function $J_b^Y$ in $^\circ C$. We choose to show winter as it highlights the peak sensitivities (see figure 5 and discussion below). The associated standard deviations (calculated over the ensemble sensitivities) show that ensemble member variation is largely within the magnitude of the sensitivity and not the location of the sensitivity. These standard deviations can be found in figure S3 in the supplementary information, although note that the color scales are not the same as in figure 4. We do not show the fresh water flux sensitivities as they are an order of magnitude smaller than those shown here. The ensemble mean and standard deviations of the sensitivities for the basins not shown here can be seen in figures S4-6 in the supplementary information.

An alternative choice for displaying the sensitivities would be to convolve them with the contemporaneous anomalies of the surface fluxes from the climatological mean. We have included some example plots of these fields in the supplementary information. These show the actual contribution of surface fluxes variations to variations in the MWFR heat content. This is a common technique when using adjoint models for attribution studies, see, for example Pillar, Heimbach, Johnson, and Marshall (2016). We choose to show the sensitivities unaltered apart from scaling by a representative standard deviation in order to show the underlying properties of the ocean. The structure of the raw sensitivity fields highlights the full range of potential processes that could influence the MWFR linearly.

It should be noted that the adjoint model does not calculate entirely independent sensitivities of the surface forcings considered here (heat flux, wind stress and fresh water flux). The bulk formulae couple these quantities together, such that the sensitivities of the net heat flux fields are not entirely independent of wind-driven mechanisms. These effects can be seen in the results of the forward perturbation experiments in section 4, where the wind stress perturbation experiments result in changes in the diagnosed heat flux. The bulk formulae in ECCOv4 r2 do not included dependence on the ocean surface velocities in the calculation of wind stress, so there are no such direct linear feedbacks on the wind-stress sensitivities. However, the coupling between surface forcings

**Table 1.** Representative Standard Deviations $\sigma_0$ used throughout, calculated from the Southern Ocean mean (S of 30°S) of the ECCOv4 fields' standard deviations.

| Property Symbol | Property Name | Standard Deviation |
|---|---|---|
| E-P-R | Surface Fresh Water Flux | $2.0\text{x}10^{-8}$ m s$^{-2}$ |
| $Q_{\text{net}}$ | Surface Heat Flux | 60 W m$^{-2}$ |
| $\tau_E$ | Zonal Wind Stress | 0.08 N m$^{-2}$ |
| $\tau_N$ | Meridional Wind Stress | 0.06 N m$^{-2}$ |
| $\theta$ | Potential Temperature | 0.3 °C |

in the forward, non-linear model, is much stronger due to strong non-linear feedbacks within the mixed layer, whereas the coupling in the adjoint model is for linear perturbations only. Thus, the adjoint sensitivities show sensitivities independent of non-linear feedbacks, and whilst it may be theoretically possible to decouple the surface stresses entirely, this is beyond the scope of this paper.

Additionally, it should be noted that these are sensitivities of a fixed volume: the sensitivities as calculated cannot indicate whether a warmer mixed layer might shallow and therefore decrease in volume, and thus decrease in overall heat content. This is discussed further in section 4. This may also be why the sensitivities to fresh water fluxes are negligible when the influence of fresh water fluxes on mode waters has been observed in, for example, Cerovečki et al. (2019); Close et al. (2013). Salinity changes are likely to have a strong influence on the density and therefore volume of mode waters, but not directly on the temperature of our fixed volume MWFRs.

$Q_{\text{net}}$ is defined as positive for heat flux from the ocean to the atmosphere. Thus *negative* sensitivities indicate that a *reduction* in $Q_{\text{net}}$, i.e. *less* heat from ocean to atmosphere, results in an increase in the objective function, i.e. MWFR heat content, and *positive* sensitivities indicate instead that an *increase* in $Q_{\text{net}}$ will result in an increase in the objective function. The largely negative sign of the $Q_{\text{net}}$ sensitivities (figure 4, upper row) is thus not unexpected, showing that a cooling of the ocean surface in these regions results in a cooling of the MWFR. The location of the peak sensitivity is largely on top of, or at previous lags, "upstream" of the location of the median objective function, inferred by the expansion of the sensitivities along well-known oceanic pathways with increased lag. Again, this is not unexpected and indicates that simply heating/cooling the source waters for the MWFR results in heating/cooling of the MWFR itself. These features are common across sensitivities to $Q_{\text{net}}$ for all lags and in each of the three basins (the Pacific and Atlantic can be seen in figure S4 in the supplementary information), and can be used to identify the source regions of the MWFRs.

The wind stress sensitivities (figure 4, middle and lower rows) have a very different structure to the $Q_{\text{net}}$ sensitivities, notably there are significant sensitivities of both signs. Dipole-type structures are common across all such wind stress sensitivities (not just those shown here), with features centered on the boundaries of the objective functions and over source water regions upstream. These types of features we associate with convergence/divergence and thus vertical Ekman pumping/suction of water.

Additionally, the sensitivities to zonal wind stress stretch both north into the subpolar gyres and south across the ACC for all basins. This indicates a direct connection with the strength of the wind-driven sub-polar gyres and possible links with ACC transport – an increase/decrease in zonal wind stress could imply an increase/decrease in meridional Ekman transport across the ACC, or a change in the tilt of the isopycnals resulting in a change in zonal ACC transport.. Other common features are what appear to

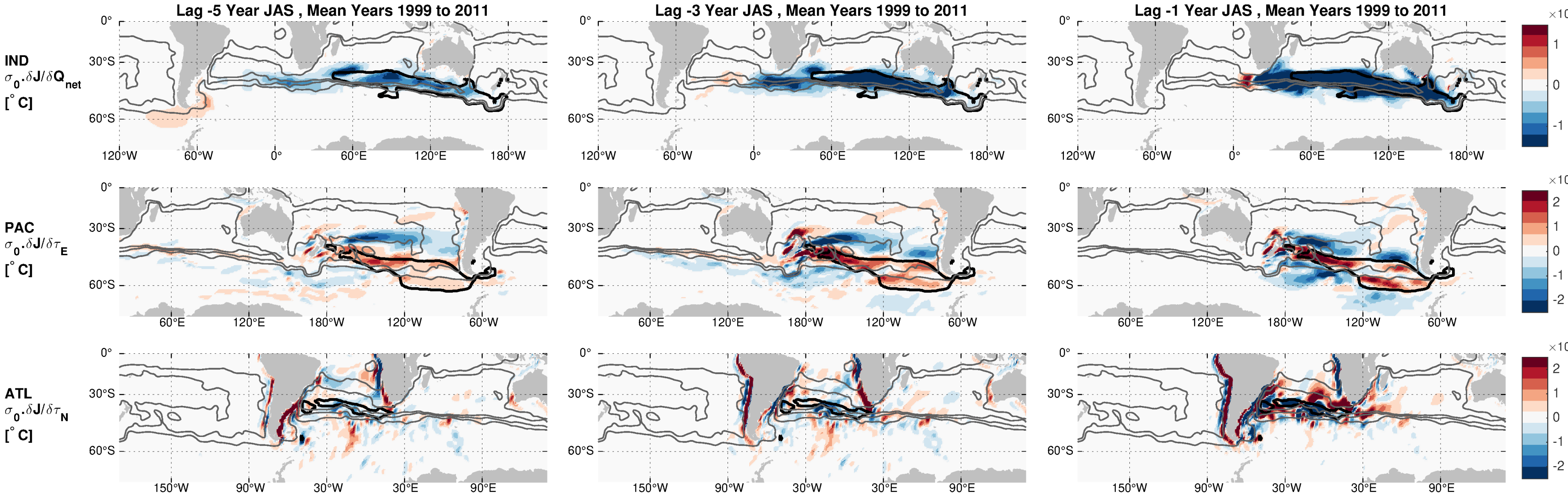


**Figure 4.** Example sensitivity fields showing the range and general properties of adjoint model simulations: Ensemble mean winter (Jul-Sep) sensitivities for surface properties at lags of 5, 3, and 1 years (left, middle, and right columns respectively). The upper row shows sensitivities of the Indian MWFR (median location indicated by black contour) to surface heat flux $Q_{\text{net}}$. The middle row shows sensitivities of the Pacific MWFR (median location indicated by black contour) to zonal wind stress $\tau_E$. The lower row shows sensitivities of the Atlantic MWFR (median logcation indicated by black contour) to meridional wind stress $\tau_N$. The grey contours indicate the -17, 0, and 30 Sv mean barotropic streamlines. The associated ensemble standard deviations and sensitivities for the basins not shown here can be found in the supplementary information.

be dynamical links with boundary current regions – dynamic because the sensitivities are not in source regions and because the sensitivities often propagate through space over time either along or away from boundaries in patterns similar to topographic, Kelvin, and Rossby waves. This can be seen more easily in the animations provided in the supplementary information and is discussed further in section 3.2.

The negative sensitivity of the Pacific MWFR to zonal wind stress on 1-3 year lags in the region of 120W to 90W and South of 60S (the Amundsen Sea, see figure 4) is consistent with the results of Close et al. (2013), who find a link between an increased Amundsen Sea Low (ASL, resulting in weaker zonal wind stress) and warmer SAMW. However, this sensitivity is relatively weak compared with zonal and meridional (see figure S6 in the supplementary information) wind stress sensitivities over, to the north of, and upstream of the MWFR, whilst Close et al. (2013) believe the ASL is significant in determining SAMW properties. This may be because although the region shows low sensitivity relative to other regions, the actual wind-stress changes in the region are significantly larger than those in other regions, although this does not appear to be the case for climatological anomalies, see figure S7. The fact that regions of high sensitivity may not be regions of high variability is discussed further in section 5.2. The lack of a stronger link with wind stress to the south of the ACC core in these sensitivities may be because the dynamic pathways linking this region with the MWFRs are too weak, consistent with the fact that the ECCOv4 model has too weak northward transports close to the Antarctic continental shelf, see discussion in Jones et al. (2019).

The wind stress sensitivities are consistent with the findings of Iudicone, Rodgers, Schopp, and Madec (2007), who find that the export of mode water from the Pacific basin is controlled by the basin-wide meridional pressure gradient – reflected in the basin-wide dipoles in zonal wind stress sensitivities seen here – and by the generation of eastward and westward propagation of Rossby, coastal Kelvin, and equatorial Kelvin waves, also seen here. This suggests that the sensitivity of the export of mode water to the basin-wide pressure gradient (as found by Iudicone et al., 2007) could be related to the sensitivity of the heat content of the mode water in its formation region to the same basin-wide properties (as demonstrated here). In other words, a change in the the zonal wind stress could alter basin-wide pressure gradients, alter the heat content of the mode water, and also lead to, directly or indirectly, changes in the export of that mode water. However, the adjoint model cannot directly represent changes in mixing caused by changes in stratification due to surface flux changes, so this cannot be fully tested in our model.

To compare sensitivities over time, we first calculated scaled domain-integrated absolute sensitivities over time for each basin, i.e. the absolute value of the sensitivity is taken before integration, meaning positive and negative sensitivities *do not* cancel out. Thus, the integrated absolute sensitivity is the maximum possible impact on the objective function if perturbations are applied with the same sign and magnitude as the the sensitivities themselves. In each basin, sensitivity to $Q_{\mathrm{net}}$ is highest at lag 0 and then decays with a strong seasonal cycle as the lag increases, peaking each winter (figure 5). Here lag 0 is defined as the beginning of the objective function integral, i.e. at the start of July – see (3) – and so non-zero sensitivities are possible at positive lags. Sensitivity to wind stress decays more slowly and has a very slight seasonal cycle, relative to the heat flux sensitivity, which it also appears to be out of phase with. The seasonality is determined by the competing seasonal influences of positively and negatively signed regions, see figure 6.

With our chosen scalings, sensitivity to $Q_{\mathrm{net}}$ initially dominates in the Pacific basin, with wind stress sensitivity dominating after around 1 year lag. Wind stress sensitivity dominates in the Atlantic basin, and largely dominates in the Indian basin apart from during the objective function integration period (positive lags), where the $Q_{\mathrm{net}}$ ensemble mean sensitivity just dominates. However, the sensitivity that dominates at any given time is dependent on the scaling applied. Scaling the sensitivities instead by the clima-

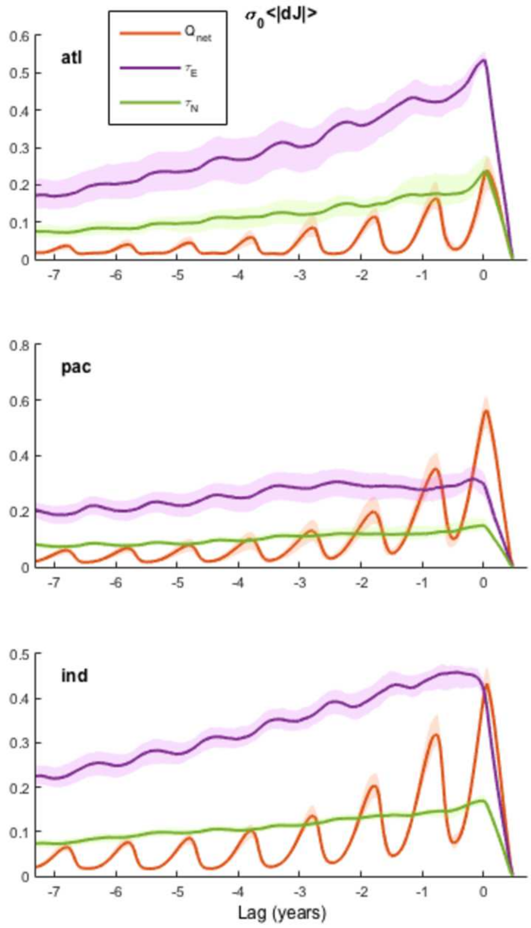


**Figure 5.** Wind stress largely dominates basin-integrated absolute sensitivities: Integrated absolute sensitivities to surface forcings by basin (top to bottom, as labeled), scaled by a representative standard deviation $\sigma_0$ and normalized, plotted against lag relative to the start of the objective function. Colors indicate surface net heat flux ($Q_{\mathrm{net}}$, red), and zonal/meridional wind stress ($\tau_{E/N}$, purple/green). The shaded area indicates the ensemble envelope (spanning the ensemble max and min values, *not* a standard deviation or similar) and thick lines the ensemble mean.

tological anomaly results in a relative increase in the $Q_{net}$ sensitivity, see supplementary information figure S8, although the overall pattern of $Q_{net}$ sensitivities dominating at short lags (0-1 years) and wind stress dominating at longer lags still holds.

The integrated sensitivities show remarkable similarity between the basins, while differences are likely due to the different locations and sizes of the MWFRs in each basin. The Atlantic MWFR is relatively far north, where it is strongly influenced by the wind-driven Atlantic sub-tropical gyre, and thus wind stress influences are relatively strongest here. The Pacific and Indian MWFRs are both further south within the ACC, and have relatively lower sensitivity to wind stress compared with heat flux. The Indian MWFR has the largest volume, see figure A.1, which may also affect the relative sensitivities.

These results indicate that the surface heat flux has the largest impact during winter on mode water formed during that same winter, and thereafter seasonally affects subsequent winters, but to a lesser and lesser degree. The large magnitude of the seasonal cycle means that heat fluxes in past winters have a much stronger influence on MWFRs than intervening summers, even years apart. Wind stress, however, can produce a similar or larger impact than heat flux for years to come, with relatively less seasonal variation, perhaps linked to the dynamical, longer-range nature of the connection with the MWFRs. More explicitly,dynamic processes such as changes in the Ekman pumping over source regions; changes in the ACC or other currents' strengths; the generation of Rossby/Kelvin waves, could influence the MWFRs for many years, regardless of the local mixed layer depth in the MWFR itself. These findings are similar to the results of Jones et al. (2019), who find the heat content of water that subducts from the MWFR is strongly controlled by the sub-tropical gyre strength and structure, which is in turn strongly related to windstress over the gyre for the previous 3-4 years.

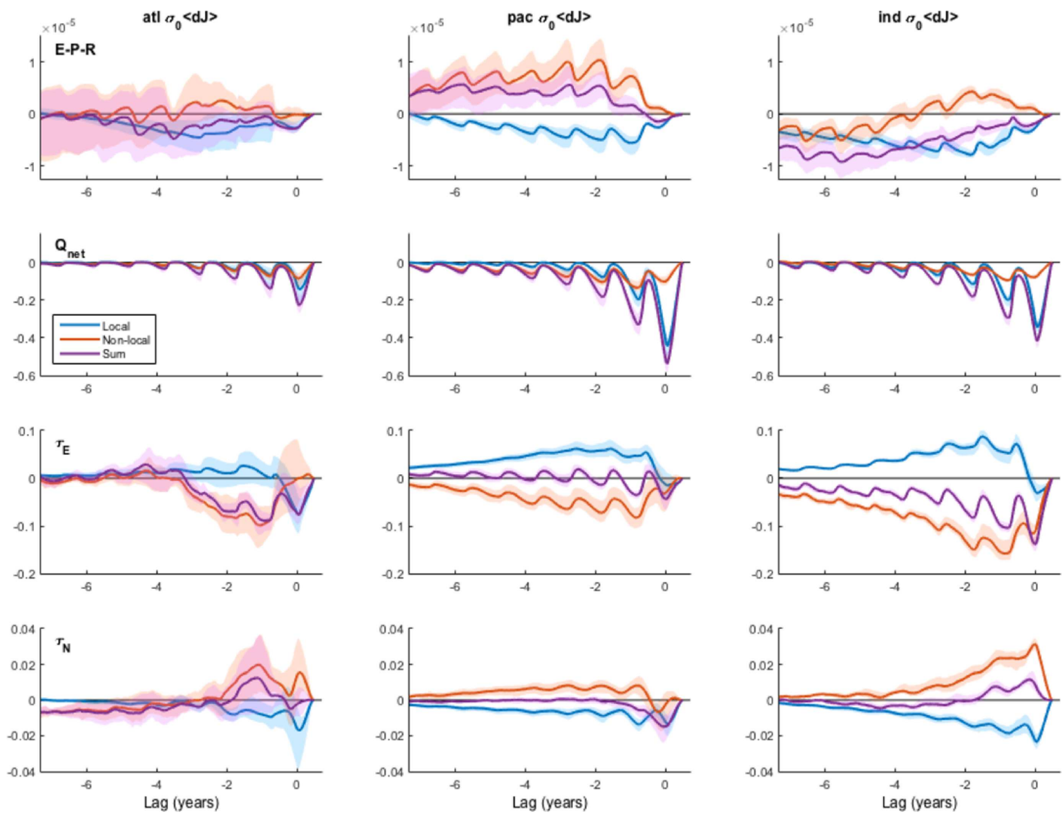


**Figure 6.** Local heat flux sensitivities dominate on short time scales, both local and non-local wind stress sensitivities are important at a range of time scales: Domain integrated sensitivities split by surface forcings (top to bottom, as labeled) and by basin (left to right, as labeled), scaled by a representative standard deviation and normalized, plotted against lag since the start of the objective function. Colors indicate the local sensitivities (within objective function mask, blue lines), non-local sensitivities (outside mask, red lines) and the sum of the two, i.e./ total sensitivities (purple lines). The shaded area indicates the ensemble envelope (spanning the ensemble max and min values) and thick lines the ensemble mean.

As well as absolute sensitivities, we also calculated and compared integrated sensitivities with signs intact, and so opposite-signed sensitivities canceled each other out.

We also split the sensitivities by local sensitivities (within the objective function mask), non-local sensitivities (outside mask), which sum to the total integrated sensitivity. These integrated sensitivities give an indication of the predicted impact on the objective function of a domain-wide positive increase in the surface forcing – this will cause an increase in the objective function due to positive sensitivity regions, and a counteracting decrease due to negative sensitivity regions. The sensitivities in the objective function region ('local') are often differently signed to those outside ('non-local').

For completeness, sensitivities to surface fresh water fluxes are included in figure 6 (upper row). In all three basins, local sensitivities dominate for the first year, peak in magnitude at some point between one and three years lag before decaying away, with a clear seasonal cycle. Local sensitivities continue to dominate in the Atlantic and Indian basins at longer lags, although there is large variability between ensemble members in the Atlantic. In the Pacific basin, non-local sensitivities dominate at lags greater than one year, and do not appear to be decaying significantly after eight years of lag, although again there is relatively large variability. There is a clear seasonal cycle apparent in all sensitivities. Thus, local sensitivities to fresh water forcing are important at timescales of up to three years, and non-local sensitivities can remain relatively large, but with large variability between basins and ensemble members.

The sensitivities to $Q_{\text{net}}$ (figure 6, second row), being largely single-signed, show very similar behavior to that in figure 5, with a pronounced seasonal cycle and strong decay over time. The local sensitivity dominates for the first year or two in all basins, before the non-local begins dominate in the Atlantic and Pacific basins. However, the local sensitivity continues to dominate at longer lags in the Indian basin, likely because the Indian MWFR has the largest volume and so the 'local' region is relatively larger, see figure A.1.

For sensitivities to both zonal and meridional wind stress (figure 6, third and fourth rows), the local sensitivity in each basin dominates for one year (Atlantic and Pacific basins), or not at all in the Indian basin. The local and non-local sensitivities are largely of opposite sign, related to the dipole structures seen in figure 4. There is also a larger seasonal cycle apparent, especially in the sensitivities to zonal wind stress $\tau_E$, with local and non-local sensitivities being out of phase with each other, leading to the much smaller seasonal cycle when looking at the absolute sensitivities in figure 5.

The time dependence of the sensitivity to heat fluxes suggests a process very much dominated by mixed layer properties - the sensitivity is largest in the winter when mixed layers are deepest, and the relative importance of past years decreases in time, with sensitivities at two years lag around half of that at zero years. This is consistent with the fields in figure 4 that show sensitivities confined to the objective function region (where the mixed layers are deepest) and upstream. The slower decay and relatively weaker seasonal cycle in the wind stress sensitivities also point to the influence of more dynamical processes which are not strongly linked to local mixed layer depths, and have stronger influences at larger lags.

The seasonal basin-wide mean mixed layer depths (means within each basin south of 30°S) correlate tightly with the $Q_{\text{net}}$ sensitivity seasonal cycles in all basins, in all years, in all ensembles (max $R^2$ within ensemble members = 0.98–0.99). They also correlate well with the seasonal cycle of the integrated wind stress sensitivities in the Indian basin (ensemble max $R^2$ =0.87–0.97). Looking at ensemble member to ensemble member variability in peak sensitivities, the link with mixed layer properties is less clear. There is a statistically significant, but weak ($R^2 = 0.33$) correlation between the annual maximum of the whole Southern Ocean mean MLD (south of 30°S) and the ensemble member peaks in total $Q_{\text{net}}$ sensitivity (summed over the three basins), but not for individual basins. In the Indian basin, there are statistically significant correlations between ensemble member peak absolute wind stress sensitivities and the annual maximum Indian ocean mean MLD ($R^2 = 0.55/0.68$ for $\tau_{N/E}$).

These correlations imply the seasonal variation in $Q_{\text{net}}$ sensitivities are almost entirely controlled by the mixed layer, but that year to year changes in peak sensitivities are not so clearly related to mixed layer properties. We speculate that this could be because year to year changes integrate influences over many years, so that the relationship with individual years is not as clear. Conversely, whilst the Atlantic and Pacific wind stress sensitivities are not strongly correlated with mixed layer properties on seasonal and inter-annual timescales, the Indian basin wind stress sensitivities show a link with mixed layer properties on both timescales, although it is the integrated sensitivity that shows seasonal links, and the absolute sensitivity that shows inter-annual links. The integrated wind stress sensitivities show a more pronounced seasonal cycle than the absolute, cf. figures 5 and 6, showing that the overall sensitivity to a domain-wide single-sign increase in wind stress is controlled by mixed layer properties on a seasonal time-scale. However, on an inter-annual time-scale, it is the absolute sensitivity that is partially controlled by peak mixed layer depths.

### 3.2 Sensitivities to Kinematic and Dynamic Potential Temperature

As in Marotzke et al. (1999) and Jones et al. (2018), we analyzed the sensitivities of the objective function to potential temperature by splitting it into sensitivities due to changes in temperature along isopycnals (referred to as kinematic changes) and changes in temperature that result in density changes (referred to as dynamic changes).[2] This is achieved by considering our objective function as a function of both density and potential temperature, i.e. $J = J[\rho(\theta, S), \theta]$, where $\rho$ is density and $S$ is salinity. Thus the sensitivity to potential temperature can be written

$$\left(\frac{\partial J}{\partial \theta}\right)_S = \left(\frac{\partial J}{\partial \rho}\right)_\theta \left(\frac{\partial \rho}{\partial \theta}\right)_S + \left(\frac{\partial J}{\partial \theta}\right)_\rho, \tag{4}$$

where the first term on the RHS is identified as the dynamic component of the sensitivity, and the second term the kinematic. We then use the definitions of the coefficients of thermal expansion $\alpha$ and of haline contraction $\beta$:

$$\alpha \equiv -\frac{1}{\rho}\left(\frac{\partial \rho}{\partial \theta}\right)_S \text{ and } \beta \equiv \frac{1}{\rho}\left(\frac{\partial \rho}{\partial S}\right)_\theta, \tag{5}$$

to write

$$\left(\frac{\partial J}{\partial S}\right)_\theta = \left(\frac{\partial J}{\partial \rho}\right)_\theta \left(\frac{\partial \rho}{\partial S}\right)_\theta = \beta\rho\left(\frac{\partial J}{\partial \rho}\right)_\theta, \tag{6}$$

and so the dynamic sensitivity can be written:

$$F_{\text{dyn}} = \left(\frac{\partial J}{\partial \rho}\right)_\theta \left(\frac{\partial \rho}{\partial \theta}\right)_S = -\frac{\alpha}{\beta}\left(\frac{\partial J}{\partial S}\right)_\theta. \tag{7}$$

[2] The definition of kinematic and dynamic changes may remind the reader of 'spice' and 'heave'. These are most often used to refer to the decomposition of temperature changes in time at a fixed depth into changes on neutral density surfaces (spice) and changes due to the motion of these surfaces (heave)(see, for example Bindoff & Mcdougall, 1994). Whilst this decomposition is conceptually similar, the definitions are different from our decomposition here. We are considering the changes in our objective function J, a non-trivial function of temperature, at constant salinity. Kinematic anomalies are possible changes in potential temperature at a fixed density at one point in time, which is not quite the same as 'spice' anomalies, normally defined as a change over time of potential temperature at a fixed density. Dynamic anomalies are related to changes in density at fixed salinity, which is similar to but not the same as 'heave', related to the change in the height of a density surface over time.

Then, rearranging (4) we can write the kinematic sensitivity as:

$$F_{\mathrm{kin}} = \left(\frac{\partial J}{\partial \theta}\right)_S + \frac{\alpha}{\beta}\left(\frac{\partial J}{\partial S}\right)_\theta . \tag{8}$$

Thus we calculated both dynamic and kinematic sensitivities from the sensitivities to potential temperature and salinity $[(\partial J/\partial \theta)_S$ and $(\partial J/\partial S)_\theta]$ output directly from the MITgcm adjoint model in combination with the factor $\alpha/\beta$ calculated from the model output potential temperature on the same two week average time-steps using the TEOS-10 Matlab toolbox (McDougall & Barker, 2011). Note that, unlike the sensitivities to surface fields, each dynamic/kinematic sensitivity snapshot is a three-dimensional field that also depends on depth.

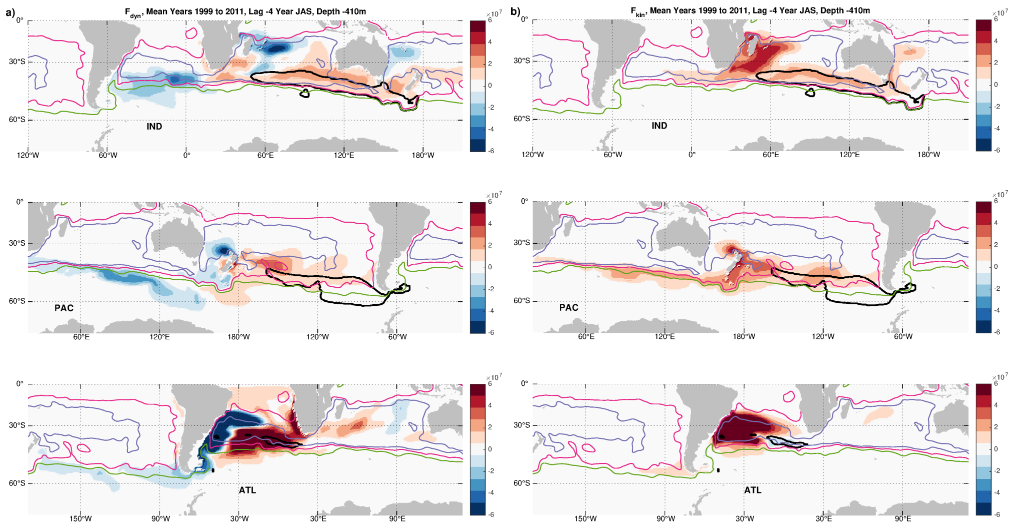


**Figure 7.** Example dynamic and kinematic sensitivities highlight their different properties: Sensitivities to a) dynamic and b) kinematic potential temperature changes at a fixed depth of 410m, fixed lag of 4 years, in all three basins (top to bottom). The black contour indicates the median location of the objective function at each depth, and as previously, the contours indicate the -17, 0, and 30 Sv mean barotropic streamlines. The associated ensemble standard deviations can be found in the supplementary information. Sensitivities are scaled by $1/\rho_0 c_p$ and are unitless.

We calculated ensemble mean dynamic and kinematic sensitivities for the same experiments as previously discussed, where the objective function is the heat content of MWFRs. The sensitivities were scaled by $1/\rho_0 c_p$ and so are unitless, i.e. the amount by which the objective function would increase in $°C$ for a dynamic/kinematic rise in potential temperature of $1°C$. The kinematic sensitivities peak at an average depth of 410m, and the dynamic sensitivities peak at an average depth of 3km (not shown). We choose to plot both quantities at 410m as the potential temperature anomalies are 2 orders of magnitude larger at this depth (not shown).

The ensemble mean dynamic sensitivities at 4 years lag and 410m depth have significant distinct single-signed regions of both signs, as well as dipoles (figure 7a, other lags and shallower depths are similar, but at longer/shorter lags extend further/less far [not shown]). Positive dynamic sensitivity indicates that decreasing the density (deepening the density surfaces) at this point would result in an increase in the MWFR heat content, and conversely negative dynamic sensitivity indicates increasing the density (raising the density surfaces) would result in an increase in the MWFR heat content. Within the objective function volume (indicated by the black contours) the sensitivity is largely positive, implying downwelling will produce an increase in the MWFR heat content. As can be seen with comparison with figure 7b, much of the strong dynamic sensitivity is placed along the same location as source waters, indicated by strong kinematic sensitivities, but they also stretch further south across the ACC. In the Indian sector, as in the Pacific sector, there are dynamic sensitivities of both signs, both over source regions and extended around these regions. These can be interpreted as highlighting that changes in the strength and structure of the ACC and sub-tropical gyres can draw more or less heat into the mixed layer, although, as previously discussed, any such link would need to be confirmed in a forward run.

The dynamic sensitivity of the Atlantic sector shows a strong dipole directly in the region of the objective function, and the structure of sensitivities is similar at shallower depths. This pattern rotates in place over time in an anti-clockwise or cyclonic direction, consistent with the westward motion of sensitivity peaks centered at $\sim$30°S and the eastward motion of sensitivity peaks at $\sim$40°S. This is another indication that the ECCOv4 Atlantic mode water pool is strongly controlled by the dynamics of the Atlantic sub-tropical gyre.

In general, dynamic sensitivities for all three sectors are a mix of positive and negative regions, with strong links to continental boundaries. Viewed as animations, one can see that there are many dynamical features that are generated at continental boundaries and then propagate along or away from these boundaries in behavior that resembles that of Kelvin, Rossby, and topographic waves. Some animations can be viewed in the supplementary information.

The mean kinematic sensitivities at 4 years lag and 410m depth, by contrast, are largely single signed (figure 7b, sensitivities at shallower depths and at longer/shorter lags are very similar but extend further/less far upstream [not shown]). The Indian and Pacific pools, being close to the northern ACC boundary, are affected by kinematic temperature changes upstream in the ACC, stretching around half its path at 4 years lag. The Indian MWFR is most strongly linked with the Agulhas and Agulhas Return Current regions, as well as more weakly with the East Australian Current region. The Pacific MWFR also shows the strongest links with New Zealand boundary current region. Conversely, the Atlantic pool is shallower and further north, more firmly in the sub-tropical gyre, and as such is highly sensitive to local gyre kinematic temperature changes rather than changes in the ACC. As kinematic temperature changes take place on isopycnals, the sensitivities strongly resemble a passive tracer sensitivity and so reflect the influences of direct heat fluxes or irreversible mixing. In fact, one can directly calculate passive tracer sensitivities in the adjoint model, and they are highly correlated with the kinematic sensitivities at the depths of the objective function (see figure S6 in supplementary information). As we consider longer timescales, kinematic sensitivities weaken and are found further away along source paths.

Similarly to section 3.1, we calculated the domain-integrated dynamic and kinematic sensitivities (with signs intact) for each basin, and split the integrals into local (within objective function volume) and non-local (outside objective function volume), which sum to the total integrated sensitivity. All three basins show very similar structures, see figure 8, with the differences being mainly in the timing of the peaks of the various integrals.

The dynamic sensitivities are generally smaller than the kinematic sensitivities, with peak kinematic sensitivities an order of magnitude higher than peak dynamic sensitivities in all basins (figure 8). The local dynamic sensitivities are all positive and peak within two years, decaying with time after. The non-local dynamic sensitivities all begin negative (indicative of the dipole structures seen throughout the dynamic sensitivity fields, see figure 7b), but then largely become positive and grow with increasing lag (although

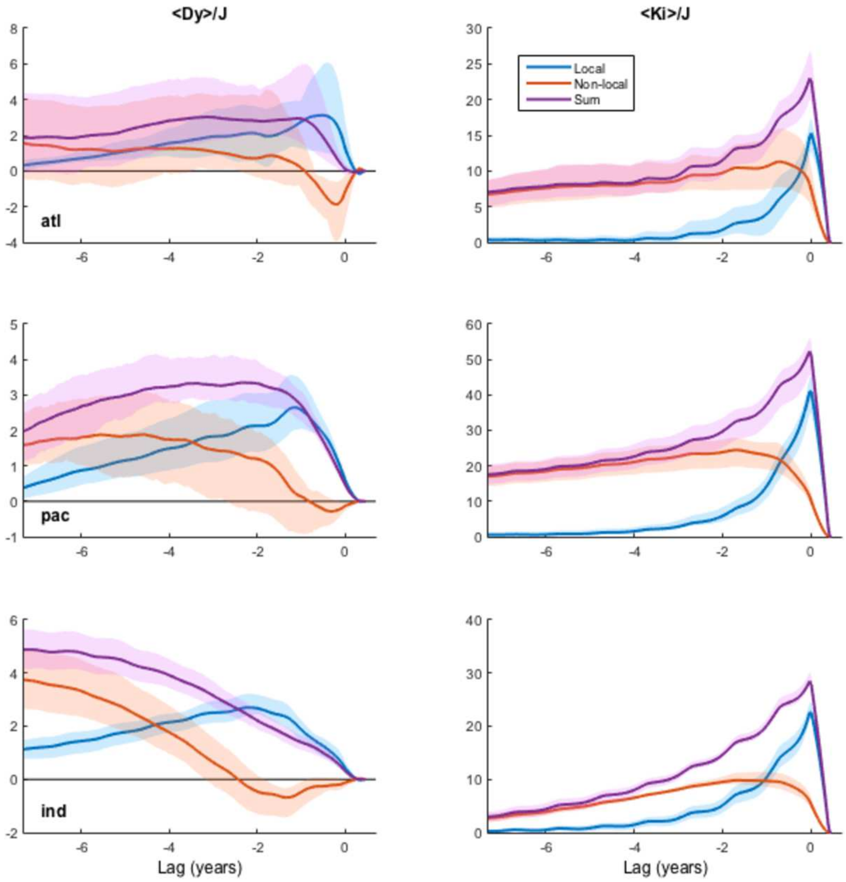


**Figure 8.** Domain-integrated kinematic sensitivities decay over time, but dominate over domain-integrated dynamic sensitivities: Domain-integrated dynamic $\theta$ sensitivities (left), and domain-integrated kinematic $\theta$ sensitivities (right) split by basin (top to bottom, as labeled). Colors indicate the contributions from local sensitivities (within objective function mask, blue lines), non-local sensitivities (outside mask, red lines), and sum total sensitivities (purple lines). The shaded region indicates the envelope of individual ensembles, and thick lines the ensemble mean. All sensitivities have been scaled by $J_b^Y$ and are therefore dimensionless.

there is significant within ensemble variability). The Indian non-local sensitivity is still growing at 8 years lag, with the Pacific looking like the ensemble mean may have peaked and the Atlantic sensitivity unclear.

The local kinematic sensitivities peak at 0 lag then quickly decay, and the non-local sensitivity takes over as the tracer-like sensitivity moves upstream. The local sensitivities decay with $e$-folding timescales of roughly 14, 15, and 18 months for the Atlantic, Pacific and Indian basins respectively, then reach a somewhat steady minimum after 4, 5, and 8 years. The difference in timescales can be attributed to the size of the MWFRs – the mean heat contents of the MWFRs increase as the timescales increase, i.e. the Atlantic is the smallest MWFR and the Indian is the largest, see figure A.1. The total and non-local sensitivities appear to reach a peak value at around 2 years lag and to still be slowly decaying at 8 years lag.

# 4 Perturbation Experiments

Adjoint sensitivities, such as those presented in section 3, are predictions about the sensitivity of the objective functions - in our case the heat content of fixed volumes - in an adjoint linear model. Thus, we expect them to predict the linear aspect of the equivalent perturbation experiments in the full non-linear model. They are considered most useful when investigating quantities that can be expected to behave linearly, such as integrals over relatively large volumes and/or time spans. As discussed in section 1, we consider adjoint sensitivities to be a useful tool for discovering which regions and timescales are of interest, but not a replacement for fully non-linear experiments. In this section, we describe how we used the adjoint sensitivities from section 3 as a starting point for a series of perturbation experiments which were used to directly investigate the impact of changes in surface forcings on our objective function, including assessing the degree of linearity in the responses, i.e. the impact of dynamics not captured in the adjoint model.

An additional complication to comparing the linear adjoint sensitivities with non-linear perturbation studies comes from the bulk formulae. Whilst the adjoint model contains the linear feedbacks for the model surface forcings considered, perturbing the same forcings in the full model can change many different aspects of air-sea heat exchange (see discussion in section 3.1). Whilst it would be possible to alter the model code in order to perturb these variables separately, the action of the bulk formulae is to produce more realistic perturbations, as in the real ocean no such independent changes would occur. Additionally, as discussed, the non-linear forward model is expected to behave differently than the adjoint linear model; this is merely one of many factors causing them to differ, and it is informative to see the full difference between the two models.

In the results below, we followed Verdy et al. (2014) and used the combination of oppositely signed perturbation experiments to calculate the linear and non-linear responses. This allowed for qualitative and quantitative analysis of the two different types of effect, and allowed us to test our assumption that the non-linear component of our objective function is small compared with the linear. Further details of the derivation of the linear and non-linear responses can be found in A.3. We applied perturbations in the surface heat flux and the zonal wind stress fields in regions where sensitivities were relatively high, and also included a test case where strong perturbations were applied to an unresponsive region, as defined by low adjoint sensitivities.

## 4.1 $Q_{\text{net}}$ Pacific Perturbation

For our first perturbation experiment, we chose a region in the South-East Pacific identified in other studies as important for downstream Sub-Antarctic Mode Water (SAMW) properties (Naveira Garabato, Jullion, Stevens, Heywood, & King, 2009), and additionally which shows an interesting pattern of heat flux sensitivity. At two years lag, the Atlantic MWFR has a region of positive sensitivity in this region of the South-East Pacific, just upstream of Drake Passage (see figure 9a upper panel). This implies that positive heat flux perturbations in this region i.e. increasing heat loss to the atmosphere, will result in a warmer MWFR in the Atlantic in two years time (as previously stated, $Q_{\text{net}}$ is defined as positive out of the ocean). Notably there is negative sensitivity over the region of the objective function, so increasing heat loss directly over the Atlantic MWFR would result in a *cooler* MWFR in two years time.

We designed a set of four perturbation experiments to test the sensitivity of the forward nonlinear model to changes in net heat flux in this key region. The black dashed contours in figure 9a show the region over which the $Q_{\text{net}}$ perturbations were applied, in four separate step changes with magnitudes of $\pm 10$ Wm$^{-2}$ and $\pm 100$ Wm$^{-2}$, constant over the box indicated. These perturbations were applied to the forward non-linear ECCOv4 r2 model at the beginning of the model run. Additionally to the changes in $Q_{\text{net}}$, there were resultant changes in the fresh water flux E-P-R, which we do not show be-

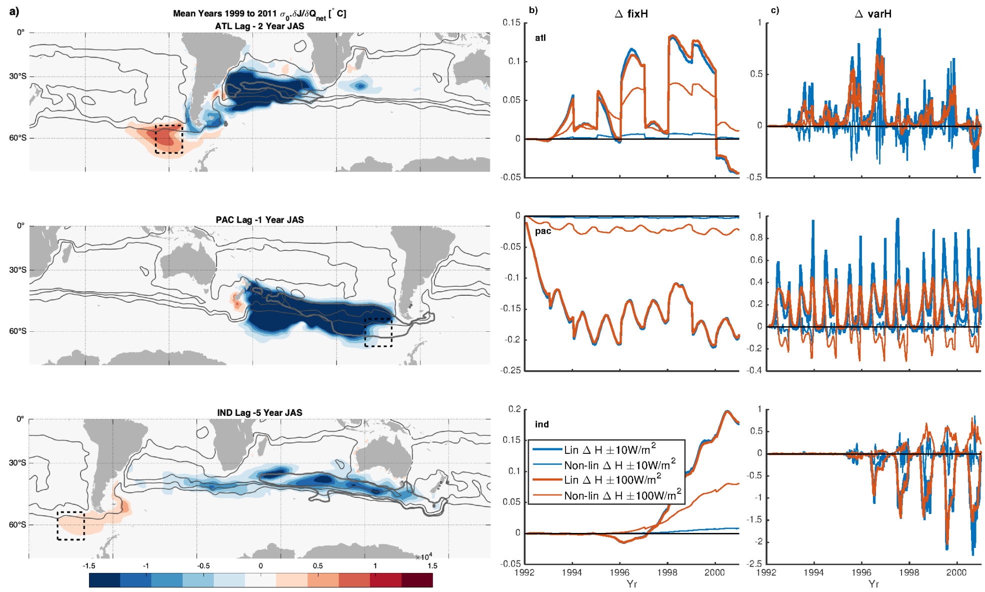


**Figure 9.** The adjoint sensitivities accurately predict the scaled linear response of the fix-MWFRs heat content: a) Ensemble mean sensitivities of mode water heat content to $Q_{\mathrm{net}}$ in various basins at lags as labelled. Thick grey contours indicated median location of objective functions, black dashed contour indicates location of $Q_{\mathrm{net}}$ perturbation (see text for details), grey contours, as before, indicate -17, 0, and 30 Sv mean SSH contours. b,c) Results of Pacific $Q_{\mathrm{net}}$ perturbation experiment, normalized linear (thick lines) and non-linear (thin lines) heat content changes divided by the perturbation magnitude, for either the fix-MWFR (b) or the var-MWFR (c), and for the $\pm$10W m$^{-2}$ (blue) or $\pm$100W m$^{-2}$ (red) experiments.

cause, as demonstrated in section 3, the sensitivities to this flux are extremely low. Thus the resultant experiment is close to being a test of the influence of $Q_{\mathrm{net}}$ independent of other surface fluxes. The perturbation region has a mean $Q_{\mathrm{net}}$ of 20 W/m$^2$ and a seasonal cycle of amplitude 120 W/m$^2$ in ECCOv4 r2, and so the $\pm$10 Wm$^{-2}$ perturbations are of similar magnitude to the mean, whereas the $\pm$100 Wm$^{-2}$ perturbations completely alter the entire seasonal cycle, shifting the region to entirely positive values year-round, or else largely negative.

The perturbation region sits over the Pacific MWFR (see figure 9a, middle panel), where the sensitivity of the Pacific MWFR is large and negative, showing that increasing the heat flux from ocean to atmosphere is an efficient way of cooling this region. At five years lag, the Indian MWFR shows weak positive sensitivity to $Q_{\mathrm{net}}$ in the perturbation region (figure 9a, lower panel). Thus, for a positively-signed $Q_{\mathrm{net}}$ perturbation in the region indicated, we expect the Atlantic objective function to show a linear increase in heat content after roughly two years, we expect an instantaneous strong decrease in heat content in the Pacific objective function, and after roughly five years we expect an increase in heat content in the Indian objective function.

We calculated the integrated heat content of the objective function regions for all four perturbation experiments over the fixed maximum winter MLD, following the definition of the objective function $J_b^Y$:

$$\mathrm{fix}H_b^Y(\theta, \mathrm{MLD}, t) = \iint^{f_b(x,y)} \int_{z=0}^{\max(\mathrm{MLD_{ASO}})} \rho_0 \, c_p \, \theta(\mathrm{r}, t) \, dx dy \, dz, \tag{9}$$

and thus the change in heat content with respect to the control simulation (the standard ECCOv4 r2 solution)

$$\Delta \text{fix} H_b^Y(t) = \text{fix} H_b^Y(\theta' - \theta, \max(\text{MLD}_{\text{ASO}}), t), \tag{10}$$

where $\theta'$ is the perturbed simulation potential temperature field and $\theta$ is that from the control simulation. The MLD was taken from the control simulation and was therefore the same depth as used in the objective function for the adjoint sensitivity experiments. We also calculated the heat content of the mode water formation regions using the objective function mask for that year, $f_b(x, y)$, but the time-varying *instantaneous* mixed layer depth in each of the simulations:

$$\text{var} H_b^Y(\theta, \text{MLD}, t) = \iint^{f_b(x,y)} \int_{z=0}^{\text{MLD}(t)} \rho_0 \, c_p \, \theta(\text{r}, t) \, dxdy \, dz, \tag{11}$$

and thus the change in the varying-volume heat content

$$\Delta \text{var} H_b^Y(t) = \text{var} H_b^Y(\theta', \text{MLD}', t) - \text{var} H_b^Y(\theta, \text{MLD}, t), \tag{12}$$

where the MLDs were taken instantaneously from the perturbed or control simulations as appropriate. To differentiate between the two volumes, the fixed-volume of the objective function and the instantaneously calculated, varying volume mode water formation region, we refer to them henceforth as the fix-MWFR and var-MWFR, respectively.

We combined the results of the positively and negatively signed experiments to produce the linear and non-linear impacts for the $\pm 10$ Wm$^{-2}$ and $\pm 100$ Wm$^{-2}$ perturbations. We chose the combinations such that the sign of the linear/non-linear changes indicate the changes for the positively signed $Q_{\text{net}}$ perturbations. Note that the heat content changes are discontinuous at the year boundaries due to the changing objective function definition for each year, as the objective function is based on the PV and MLD properties for each individual year, as discussed in section 2. The magnitude of the changes can be significantly larger for the varying-volume heat contents than the fixed-volumes as the changes in the volume (dependent on the temperature scale used) due to changes in the instantaneous MLD result in much larger heat content changes than potential temperature changes alone (see figures 9b and c, noting the different $y$-axis scales.)

One would expect the normalized linear response to be identical for both magnitudes, by definition, and this is largely true, especially for the fixed-volume heat content (see figure 9b, thick lines, which lie mostly on top of each other). There are small differences at the peaks of the varying-volume responses, likely due to the fact that the bulk formulae effects discussed previously will have introduced some non-linear changes to the perturbations that will have resulted in the positive- and negative-signed experiments not being exactly symmetric. The non-linear effects (figure 9b and c, thin lines) are smaller in general than the linear effects, but increase in the $\pm 100$ Wm$^{-2}$ case (red lines), as would be expected, becoming almost as large as the linear changes, especially in the Atlantic.

The predicted positive response is seen in the Atlantic (figure 9b and c, upper panels), with both the fix-MWFR and var-MWFR showing linear increases in heat content, starting after roughly two years. The heat content of the var-MWFR (figure 9c) shows large spikes every winter as the mixed layer deepens, but largely agrees with the sign of the heat content change of the fix-MWFR (figure 9b).

In the Pacific, at all lags a negative response was expected, and this is borne out in the fix-MWFR heat content changes (figure 9b middle panel). However, the sign of the linear change in the var-MWFR (figure 9c middle panel, bold lines) is opposite to that of the fix-MWFR: when the heat flux to the atmosphere increases, as in the $+10$ and $+100$ Wm$^{-2}$ experiments, the temperature in the fix-MWFR decreases and so does the heat content, but the heat content of the var-MWFR *increases*. This is because the cooler mixed layer deepens, resulting in more net heat content, as can be seen in figure 10.

The responses in the Indian region (figure 9b lower panel) are consistent with simple advection downstream - it takes over three years for the effect of the perturbation to reach the Indian region, and it remains much lower magnitude than either the Pacific or Atlantic effects. After this, the impact grows year on year, and similarly to the Pacific basin has an opposite-signed linear effect on the fix-MWFR and the var-MWFR. Like the Atlantic, an increase in heat loss to the atmosphere results in an overall warming of the fix-MWFR, and vice-versa. The opposite sign of the response of the fixed and varying volume heat contents is for the same reason as in the Pacific, namely that a warming mixed layer shallows and so decreases its overall heat content when the volume considered is allowed to evolve.

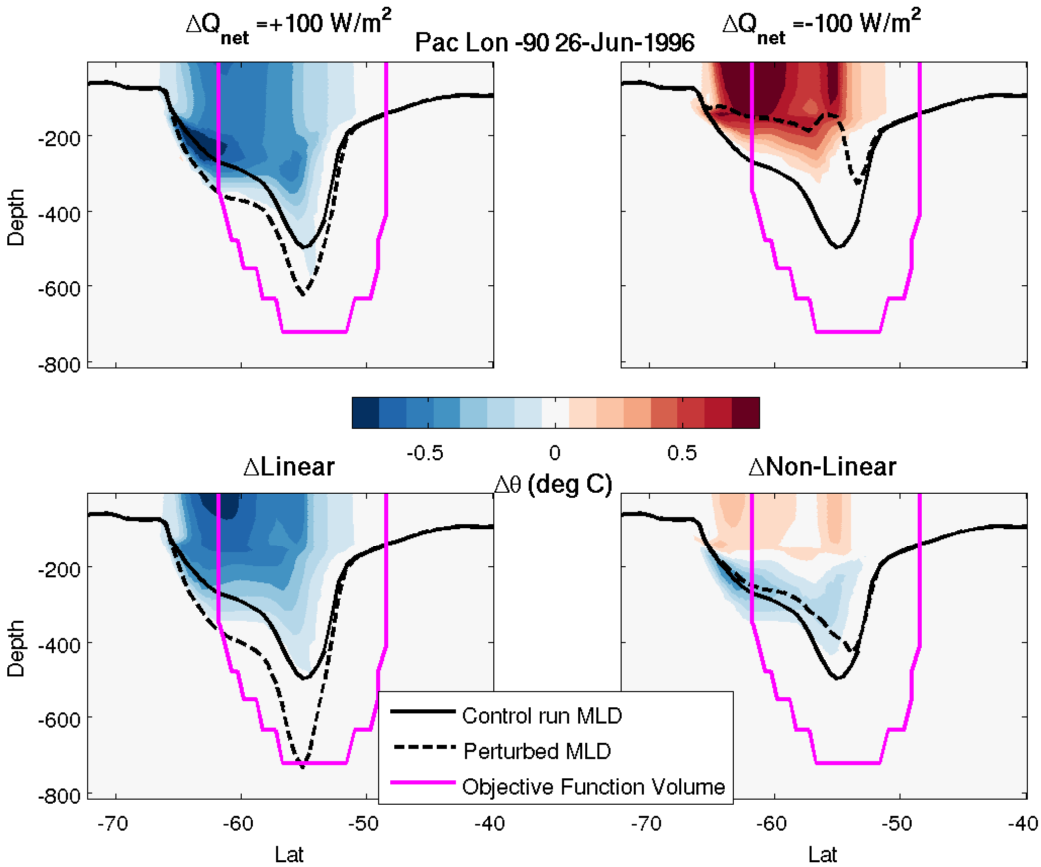


**Figure 10.** Linear changes in mixed layer depth act counter to linear changes in temperature, leading to opposite changes in heat content of the fix- and var-MWFRs: Latitude-depth snapshots of potential temperature changes (color) in the Pacific basin from the Pacific $Q_{\rm net}$ perturbation experiment in June 1996. $Q_{\rm net}$ is, as before, defined as positive from ocean to atmosphere. As labelled, the different panels show the difference from the control run for both positive and negative perturbations, and the combination of these to produce the linear and non-linear changes. The black solid lines show the control run instantaneous MLD and the magenta lines show the 1996 objective function volume (the same in every panel). The black dashed lines show the instantaneous MLD for the perturbation experiments as labelled.

Whilst the fix-MWFRs did indeed warm or cool as expected, these lead to changes in MLD that acted counter to the temperature change and resulted in a larger mixed layer heat content when the mixed layer cooled and a lower mixed layer heat content when the mixed layer warmed (figure 10). Whilst the temperature change is very linear, the change in MLD has a significant non-linear component, although the linear component is still largest. This is not surprising as the temperature response is strongly linked with the imposed linear $Q_{\text{net}}$ changes, whereas the mixed layer response is, as the name suggests, mediated by mixing, which can be non-linear in the case of convective mixing.

These results demonstrate that the adjoint sensitivities can indeed successfully predict the linear sensitivity of the fix-MWFRs in forward, non-linear simulations. However, these results also highlight that the var-MWFRs, calculated instantaneously, do not necessarily respond in the same manner as their fixed-volume counterparts. In fact the var-MWFRs seasonally respond with higher magnitudes than the fix-MWFRs. Whilst the sign may not be predicted, the fact that the heat content does significantly change is predicted. Additionally, as might be expected, larger magnitude perturbations lead to slightly larger normalized non-linear effects.

### 4.2 $\tau_E$ Pacific Perturbation

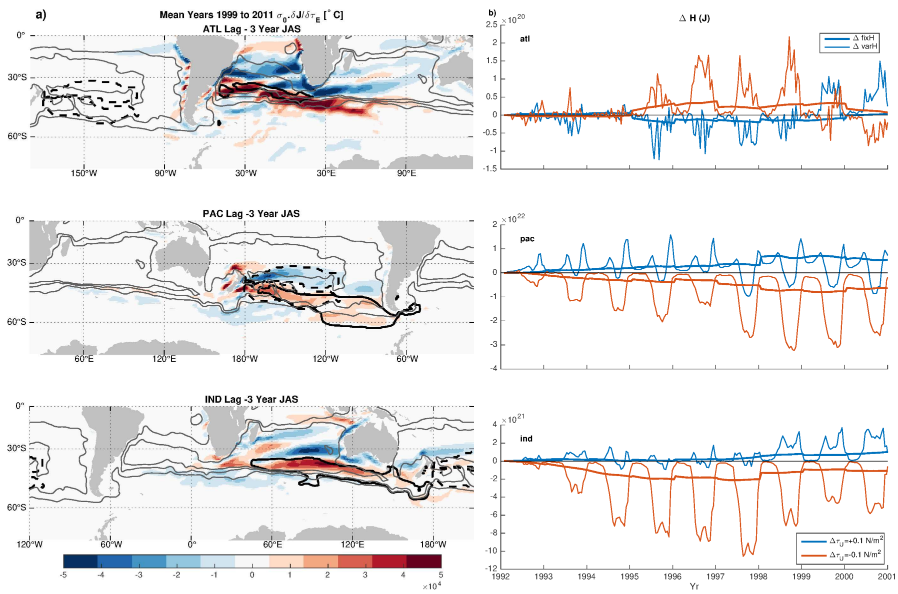


**Figure 11.** a) Ensemble mean sensitivities of mode water heat content to $\tau_E$ in various basins in winter at 3 years lag as labelled. Black contours indicated median location of objective functions, black dashed contour indicates location of $\tau_E$ perturbation (with the positive-signed perturbation matching the sign of the Pacific basin sensitivity shown here), grey contours, as before, indicate -17, 0, and 30 Sv mean SSH contours. b) Results of Pacific $\tau_E$ perturbation experiment. Heat content changes from positively-(blue lines) and negatively-(red lines)signed perturbation experiments, for either the fix-MWFR (thick lines) or the var-MWFR (thin lines).

We now consider a regional experiment perturbing the zonal wind stress, $\tau_E$. In winter and at three years lag, a clear dipole in the ensemble mean sensitivity of the Pacific MWFR to $\tau_E$ can be seen stretching east from New Zealand well into the Pacific (figure 11a, middle panel). This indicates that a zonal wind stress dipole of this sort, implying downwelling along the dipole center, would produce an increase in the heat content of the objective function region (median location indicated by the black contours). A perturbation closely matching this dipole was chosen to test this sensitivity (figure 11a, black contours) which was applied either imitating the Pacific MWFR sensitivity, with two oppositely signed regions of magnitudes $\pm 0.1$ Nm$^{-2}$, or with the signs of the two regions reversed. These two perturbations were applied separately as step changes to the forward non-linear ECCOv4 r2 model at the beginning of the model run (the start of 1992). The mean dipole amplitude in ECCOv4 is -0.04 Nm$^{-2}$ with a standard deviation of 0.03 Nm$^{-2}$ in the control run.

Additional to the changes in $\tau_E$, there were resultant changes in the heat flux $Q_{\mathrm{net}}$ due to the bulk formulae (not shown). Thus, these experiments are not an exact test of the linear response to the wind-stress perturbations applied, but can nonetheless provide interesting insights into how the linear and non-linear responses compare.

As predicted by the adjoint sensitivity, the fix-MWFR in the Pacific sector responded linearly, with an increase (decrease) in heat content over time for the positively-(negatively-)signed perturbation experiment (figure 11b, thick lines, middle row). The Indian and Atlantic fix-MWFRs responses are more non-linear than the Pacific, with an especially asymmetric response in the Indian sector, although it becomes more symmetric after 1998. Note the Alantic responses are two orders of magnitude lower than climatology (see figure A.1), reflecting its low sensitivity to the perturbation region (figure 11a, upper row).

The $\Delta$var$H$ response (figure 11b, thin lines), calculated as before from the lateral extent of the objective functions but integrated in depth to the instantaneous MLD, are largely of the same sign as the $\Delta$fix$H$ responses in all basins. This shows that, in contrast with the $Q_{\mathrm{net}}$ perturbation experiments, the mixed-layer depth changes act to increase (decrease) the volume of the MWFRs when the volumes warm (cool). This could be indicative of dynamic processes playing a part in setting the mixed layer depths. However, in both experiments, there is a seasonal decrease in the Pacific var-MWFR content during winter, perhaps related non-linear $Q_{\mathrm{net}}$ forcings via the bulk formulae.

These results show that, again, the adjoint sensitivities can accurately predict the linear response of the fix-MWFRs, with a relatively low non-linear response, especially at longer timescales. However, the response of the var-MWFR is highly non-linear.

### 4.3 $\tau_N$ Indian Ocean perturbation

The results of sections 4.1 and 4.2 confirm that the adjoint sensitivities can predict regions of objective function sensitivity in the full non-linear model. We now demonstrate the corollary, namely that perturbations in regions with low adjoint sensitivities produce weak responses in the full non-linear model. To do this we identify a region of low overall sensitivity for all MWFRS, then perturb the meridional wind stress field to see if there is a low linear response, as predicted, and what the magnitude of any non-linear response is.

A region east of Africa in the Indian ocean, which is a region of low adjoint sensitivity for both heat flux and wind stress at any time scale modeled, was chosen to test this sensitivity (figure 12, black dashed contour). A step change perturbation to the meridional wind stress field was applied either as indicated or with the opposite sign, i.e. magnitudes $\pm 1$ Nm$^{-2}$, one to two orders of magnitude larger than the ECCOv4 r2 mean and seasonal cycle amplitude (0.03 and 0.06 Nm$^{-2}$, respectively) for this region. These two perturbations were applied separately as step changes to the forward non-linear ECCOv4 r2 model at the beginning of the model run (the start of 1992). Additionally to the changes in $\tau_N$, as in section 4.2 there were resultant changes in the heat flux $Q_{\mathrm{net}}$. Whilst there are significant linear effects (figure 12, upper row), the non-linear effects are extremely large (lower row), on the order of 100 Wm$^{-2}$.

Figures 13a and b show the derived linear/non-linear responses of the fix-MWFR and var-MWFR heat contents respectively, derived as before. All basins show linear and

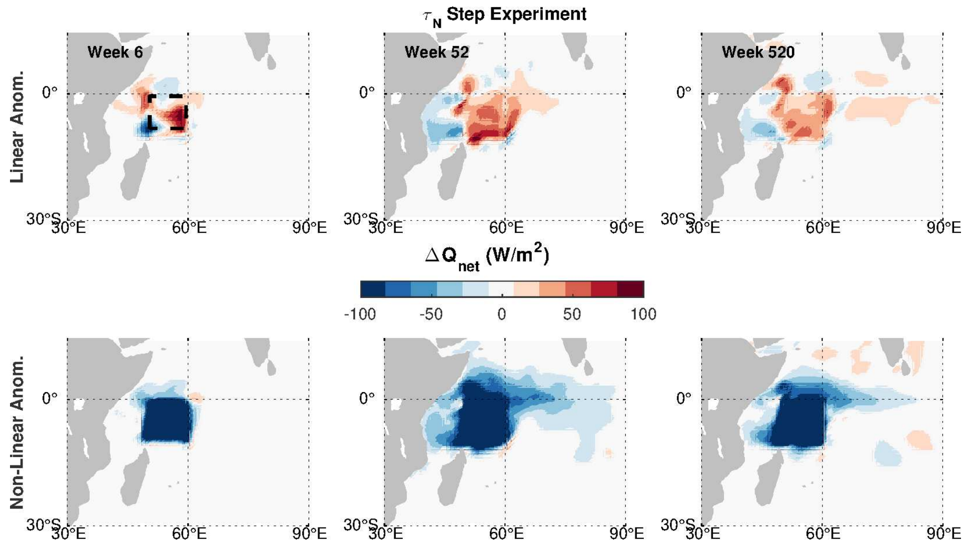


**Figure 12.** Comparison between applied wind stress and derived heat flux perturbations for E Africa experiment shows significant non-linear heat flux perturbations: Area of applied Ocean $\tau_N$ perturbation ($\pm 1$ Nm$^{-2}$ within black dashed lines) and derived Ocean $Q_{\mathrm{net}}$ perturbations via bulk formulae, linear and non-linear components (color) going forward in time, left to right.

non-linear effects of similar magnitudes, apart from the fix-MWFR non-linear impact in the Indian sector (red line, bottom panel) being significantly larger than the linear response (blue line). It should be noted that the order of magnitude of the heat contents displayed here are two orders of magnitude less than climatology (see figure A.1).

These results confirm that perturbing regions with low adjoint sensitivity produces weak linear responses (when compared with regions of significant sensitivity). Of course, this does produce a linear response in the objective function region, just one that is relatively small and of similar magnitude to the non-linear response. The responses, including the non-linear component, are at least an order of magnitude lower than those found in section 4.3, despite the larger perturbation magnitude (1 Nm$^{-2}$ vs 0.1 Nm$^{-2}$).

# 5 Summary and Discussion

We have identified locations with properties of winter mode water formation pools within the mixed layer of an observationally constrained model of the Southern Ocean (Forget, Campin, et al., 2015). Using an adjoint model, we have determined the sensitivity of the fixed-volume heat contents of these mode water formation regions (MWFRs) to surface forcings, changes of potential temperature at constant density, and changes of potential temperature that lead to changes in density, in an ensemble of 11 eight year simulations. These determine the sensitivity of the winter heat content of the MWFRs in the years 1999 to 2011 to the properties mentioned in previous years. We have highlighted the key aspects of the sensitivities here, with further results available in the supplementary information.

## 5.1 Summary of Results

Analysis of the sensitivity fields revealed that, on the eight year time scale investigated using the ECCO adjoint model, the heat content of the MWFRs is significantly affected by surface net heat fluxes and wind stress, but much less by fresh water fluxes

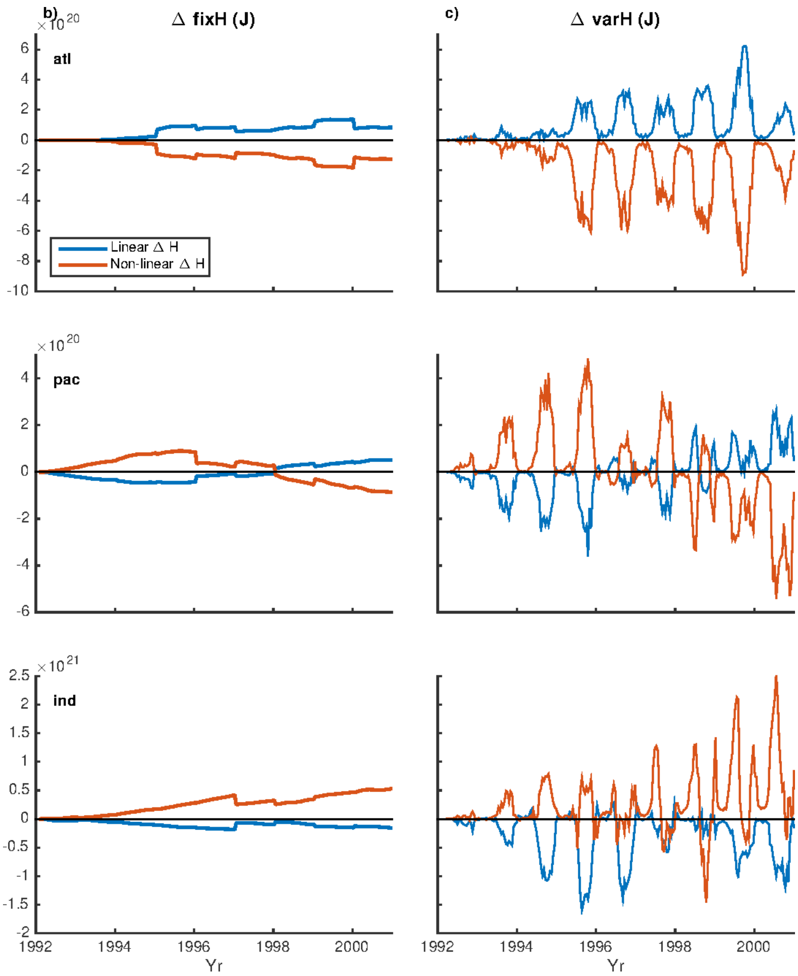


**Figure 13.** Results of E Africa $\tau_N$ perturbation experiment. Linear (blue lines) and non-linear (red lines) heat content changes, for either the fix-MWFR (a) or the var-MWFR (b). Note the different vertical scales when compared with figure 11

(discussed further on). The heat content of the MWFRs in all three basins was found to be most sensitive to local (within the MWFR), recent (within the last year) changes to surface heat fluxes. There were also significant sensitivities to non-local (outside the MWFR) wind stress changes in the past (with two to eight year lead times).

Heat flux sensitivities had a strong seasonal cycle, with the largest sensitivities occurring during previous winters, with strong correlations with the mixed layer depth seasonal cycle. This implies that surface heat fluxes are most effective at changing the heat content of MWFRs during winter, when the heat content throughout the deepened mixed layers can be influenced. The mixed layer has a 'memory' that allows for changes in one year to affect heat content the next year, indicated by the significant sensitivities in previous winters, although there is a clear decay with time that indicates the influence drops year by year, and is largely limited to changes within the last four to six years. This finding extends the role of SAMW formation preconditioning discussed in Sloyan et al. (2010) beyond a single season to over several years. It also aligns well with recent results looking at SAMW variability in the Pacific (Cerovečki et al., 2019; Meijers, Cerovečki, King, & Tamsitt, 2019) who find that while inter-annual variability in SAMW properties is largely the result of local forcing, preconditioning from upstream waters also influences prop-

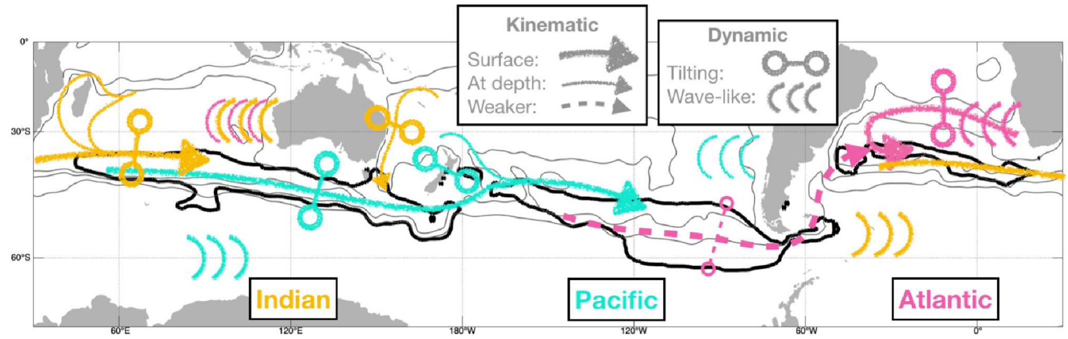


**Figure 14.** Schematic illustrating the main kinematic and dynamic sensitivities up to approximately 5 years lag for all three basins: Indian (yellow), Pacific (cyan), and Atlantic (pink). As before, thick black contours show the median location of the MWFRs and grey contours the -17, 0, and 30 Sv mean barotropic streamlines. Arrows indicate paths of kinematic sensitivities, with thinner lines indicating paths only found at depth and dashed lines showing relatively weaker paths. The circles connected by lines indicate where dynamic sensitivities resemble dipoles, where a change in isopycnal gradient will affect the MWFRs (the exact location of the symbols is not meaningful). Groups of curves indicate where wave-like patterns are found.

erties on lags of 1-2 years (not unlike in Song, Marshall, Follows, Dutkiewicz, & Forget, 2016).

Wind stress sensitivities revealed dipole patterns, and showed a less pronounced decay in magnitude with time and a less pronounced seasonal dependence, as compared with the heat flux sensitivities. Zonal wind stress sensitivities extend significantly farther south than for other properties, indicating a possible link with ACC dynamics. This is consistent with the findings of Rintoul and England (2002), who find that Ekman transport across the South Antarctic Front (SAF) south of Australia (at roughly 50S) can drive the variability in T and S properties of SAMW in this region, rather than the variation of surface fluxes.

The lack of stronger sensitivities to wind stress or heat fluxes south of the ACC could be interpreted in a number of ways. The first is that the ECCOv4 model fails to accurately represent the processes responsible for these links in observations, with, for example, too weak off-shelf transport rates (Jones et al., 2019). The second is that the regions of high variability in observations are not co-located with regions of high sensitivity, although this does not appear to be the case for the variability in the ECCOv4 solution, see fig 7. Investigating how observed variance might look when convolved with our sensitivities is part of our planned future work, see section 5.2. A third possibility is that the processes that bring strong influences from south of the ACC into the mode water regions are largely non-linear, and thus the linear sensitivities do not reveal them, although they may be present in forward fully non-linear simulations.

Finally, it may be that the influence of the waters from south of the ACC on the MWFRs is largely on the volume of the mode water pool, which is not something our sensitivities are designed to show. This would be consistent with the results of, e.g., Gao, Rintoul, and Yu (2018) who find wind stress curl changes lead to deepening or shoaling of the base of the winter mixed layer, and subsequently influence the volume of SAMW formed. Additionally, Meijers et al. (2019) find that the Pacific SAMW volume is strongly controlled by local wind stress and heat fluxes poleward of 55°S, whereas the mean temperature is not strongly linked to local surface forcings, implying it is set by advection from upstream, consistent with our results.

The analysis of sensitivities to surface forcings was supplemented by analysis of the sensitivity of the heat content of MWFRs to potential temperature changes, split into kinematic (at constant density) and dynamic (involving changes in density) components. A summary of the results is provided in figure 14. Kinematic sensitivities were, for the most part, single-signed and resemble passive tracer sensitivities and thus were largest in direct source regions for the MWFRs, with boundary currents mostly dominating over ACC sources. Dynamic sensitivities showed both signs and indicated the effects of raising/lowering density surfaces. The largest sensitivities in both cases were over source regions as well as in boundary current regions, across the Southern ACC, and in the subtropical gyres.

Given that the adjoint model is strictly linear, we chose a small set of perturbation experiments to test the validity of these results in the full forward non-linear model. We chose regions highlighted by previous studies to be of relevance for mode water properties that were also highlighted by the sensitivity fields.

These results confirmed that the adjoint sensitivities can successfully predict the linear impact of changes in surface forcings. In some regions, the sensitivities predicted the overall impact, even for relatively large perturbations, because the non-linear impacts were relatively small. The adjoint sensitivities were accurate at locating regions of high and low linear sensitivity. Additionally, low adjoint sensitivities resulted in low non-linear sensitivities.

As well as calculating the impact of the perturbations on the fixed-volume MWFRs (fix-MWFRs), we recalculated the volume of the MWFRs in the forward experiments. This allowed us to assess the role played by mixed layer depth variability on the MWFRs through time. These results showed, in some cases, that the varying-volume MWFRs (var-MWFRs) had opposite signed linear heat content changes to the fix-MWFRs. The sometimes significant differences between the fix- and var-MWFRs highlight an important limitation when interpreting the MITgcm adjoint models: they calculate the sensitivities of a fixed volume, not a water mass or layer which may dynamically alter its thickness in response to forcing.

The zonal wind stress perturbation experiment highlighted the influence of the bulk formulae on the surface properties in the model. Whilst linear, opposite-signed perturbations in zonal wind stress were applied in the two experiments, these resulted in significant *non-linear* anomalies in the surface heat flux, due to the reactions of the bulk formulae. In particular, in perturbation experiments of both signs, there was a similar, large decrease in the ocean to atmosphere heat flux.

A known issue with ocean-only models is that they do not always represent feedbacks correctly (e.g. Hyder, 2020; Strobach et al., 2018). In ocean-only models forced by atmospheric variables, which derive fluxes via bulk formulae, this manifests itself as a tight correlation between SST variability and atmospheric flux variability. Atmospheric fluxes are fixed, and so SST perturbations are strongly damped, and therefore do not advect as far or as fast at the surface as density-equivalent salinity perturbations (which are not damped). This strong coupling between atmospheric fluxes and SST is realistic on short timescales but does not allow for slower changes in ocean state. With regards to the adjoint model, this could result in an over-sensitivity of the sea surface temperature field to local $Q_{net}$ changes relative to changes in local temperature convergence on longer time scales, and should be taken into account when comparing results from any ocean-only based adjoint model with observations. The exact magnitude and time scales of this effect is beyond the scope of this work.

### 5.2 Discussion

It can also be informative to combine the adjoint sensitivities with other spatially varying fields. For example, convolving adjoint sensitivities to surface properties with two-dimensional, spatially varying, standard deviation fields can also highlight not only where sensitivities are largest, but where variability is amplified by increased sensitivity. Conversely, a region with high sensitivity may be a region of low variability, and as such play a reduced role. This might highlight where observational campaigns should be focused in order to accurately characterize the variability in a given surface forcing. Similarly, predicted changes in surface forcing under climate change scenarios may be expected to have greater impact if they occur over areas of high sensitivity.

Instead of looking at observed variability in a property, one might instead look at the spread in values between different numerical models, such as the CMIP climate model ensembles. Combining these with our adjoint sensitivities would inform on where model disagreement in surface forcings are expected to impact on predictions of MWFR heat content. This could provide motivation for model improvement in certain regions, or show which processes should be prioritized for further examination.

Additionally, one can combine sensitivity fields with anomaly (from climatological mean) fields to reconstruct the objective function in order to attribute the influences of various properties (see, for example, Pillar et al., 2016). For example, if a particular year had an unusually large MWFR heat content compared with the climatological mean, one could attribute the linear contributions to this difference using the time varying adjoint sensitivities of surface properties convolved with the time varying anomalies of these properties.

The results as presented here indicate the usefulness of adjoint models in predicting the linear sensitivity of regions of interest to surface fluxes and to interior properties. Of particular interest to the Southern Ocean research community are the findings that mode water formation regions appear to be as sensitive to non-local, dynamically linked, wind stress changes on multi-year timescales as to local, kinematically linked, heat flux changes on short time scales. With regards to modeling, it is noteworthy that the adjoint sensitivities can accurately predict the linear behavior of perturbations to the heat content of fixed-volumes in the forward, non-linear model. However, there are timescales and regions where non-linear effects can be relatively as important, and care must be taken when interpreting results when the fixed-volume approach might not be sufficiently accurate.

## A Appendix

### A.1 ECCO Mode Water Formation Region Climatology

Figure A.1 shows the climatology of the Mode Water Formation Region heat content from all 20 years of ECCOv4r2 (1992-2011), as defined in section 2. The Indian MWFR is the largest, peaking at $2.0 \pm 0.2 \times 10^{23}$ J in September, with the Pacific and Atlantic peaking at $0.9 \pm 0.1 \times 10^{23}$ J and $0.8 \pm 0.1 \times 10^{23}$ J respectively.

### A.2 Mask Comparison

Figure A.2 shows the domain-integrated absolute sensitivities to surface properties for 1999, comparing the total sensitivity of the 1999 MWFRs as described in section 2 (red lines) with the sensitivity of the 1999 Jul-Nov maximum mixed layer depth for the whole of the Southern Ocean (south of 30°S). Thus the difference between the two objective functions is the horizontal extent – the MWFRs are restricted to the areas determined by low PV values and deep mixed layers, whereas the whole Southern Ocean mixed layer stretches across the domain in the horizontal.

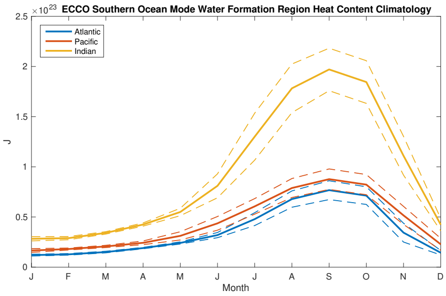


**Figure A.1.** Climatology (1992-2011) of ECCOv4 r2 Southern Ocean mode water formation region heat content, as defined by our masks in the horizontal, and integrated to the depth of the instantaneous mixed layer, see text for details. Dashed lines show one standard deviation.

The differences are most striking for the sensitivities to E-P-R, with the mixed layer sensitivities not showing the growth with increased lag that the MWFRs do, however both sensitivities remain extremely small relative to the others calculated. In general, for the heat flux and wind stress sensitivities, the mixed layer sensitivities peak at a similar or higher value at zero lag, and then decay faster with lag than the MWFR sensitivities. This is not surprising as the Southern Ocean mixed layer in general has a large surface area and is only on the order of ∼100m depth outside the MWFRs (see, for example, figure 2), and so it is expected that it will be most sensitive to recent forcings and quickly lose memory of the past. The absolute wind stress sensitivities in particular show far longer reaching behavior for the MWFRs, likely due to the presence of dipoles along the boundaries of the MWFRs.

This demonstrates that the choice to restrict our objective functions to just the MWFRs themselves produces sensitivities with a richer range of behavior and avoids over-focus on recent surface interactions.

### A.3 Linear and Non-linear Component Derivation

Given a function $f(x)$ that is infinitely differentiable at a point $a$, the Taylor series is defined as:

$$f(x) = f(a) + (x-a)\frac{f'(a)}{1!} + (x-a)^2\frac{f''(a)}{2!} + (x-a)^3\frac{f'''(a)}{3!} + ..., \tag{A.1}$$

If we assume that the a given objective function value $J$ is a function of the model surface forcings, defined by a state vector $\chi$, i.e. $J \equiv J(\chi)$, and we consider perturbations to this state vector as $\Delta\chi$, then we can approximate the perturbed objective function as an expansion about the point $\chi$ using (A.1), i.e.

$$J(\chi + \Delta\chi) \approx J(\chi) + \Delta\chi J'(\chi) + (\Delta\chi)^2\frac{J''(\chi)}{2} + ..., \tag{A.2}$$

where we can identify $J'(\chi)$ with the linear component (which is estimated by the adjoint sensitivities $\partial J/\partial\chi$) and $J''(\chi)$ with the non-linear component of $J(\chi)$. Using (A.1) to similarly define $J(\chi - \Delta\chi)$, we can combine this with (A.2) to find:

$$\frac{J(\chi + \Delta\chi)}{2} - \frac{J(\chi - \Delta\chi)}{2} \approx \Delta\chi J'(\chi), \tag{A.3}$$

$$\frac{J(\chi + \Delta\chi)}{2} + \frac{J(\chi - \Delta\chi)}{2} - J(\chi) \approx (\Delta\chi)^2\frac{J''(\chi)}{2}, \tag{A.4}$$

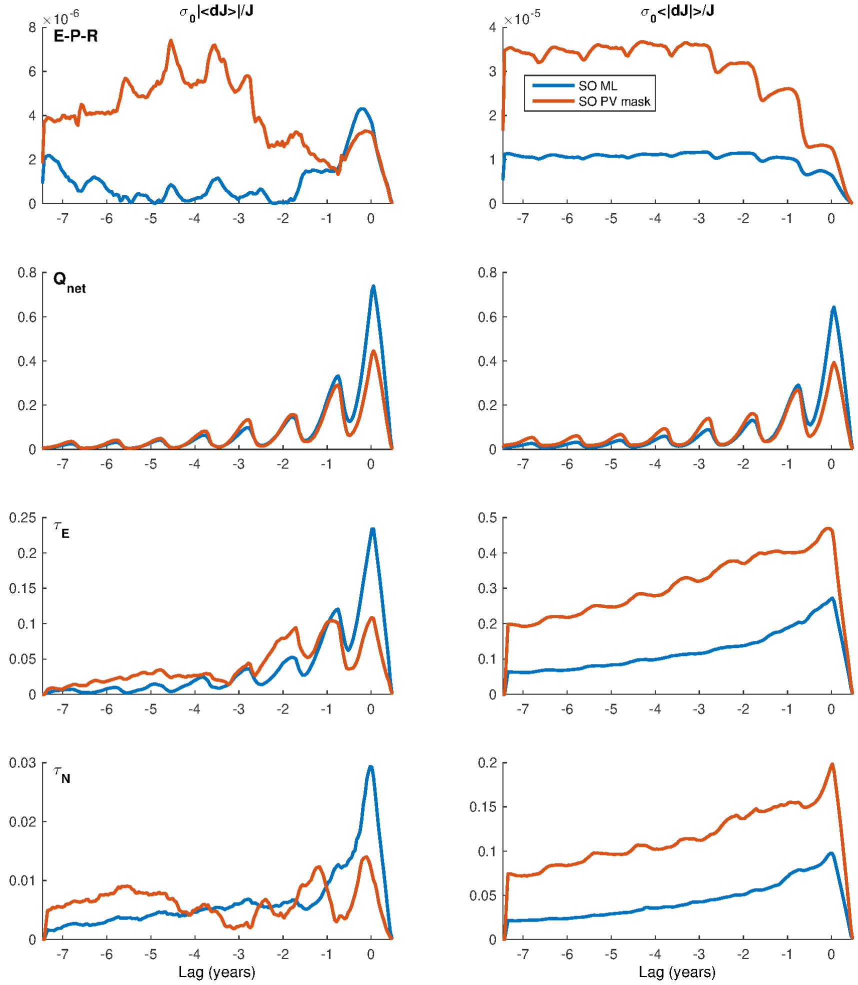


**Figure A.2.** Mean and absolute sensitivities (left and right hand plots respectively) to surface properties as labelled, fresh water flux, heat flux, zonal, and meridional wind stress, top to bottom. Blue lines show an objective function of the whole Southern Ocean mixed layer depth Jul-Nov 1999 maximum. Red lines show an objective function of the whole Southern Ocean 1999 MWFRs – with the horizontal extent determined by the masks described in section 2 and the vertical extent the Jul-Nov maximum mixed layer depth. Sensitivities have been scaled by the representative standard deviations and the value of the objective function $J$, and then normalized.

assuming that $J'''(\chi)$ and higher order terms $<<\ J(\chi), J'(\chi)$. Thus, by carrying out the perturbation experiments with state vectors $\chi \pm \Delta\chi$, we can estimate the linear and non-linear behavior of the objective function and test this assumption. We can similarly identify any model variable as a function of the model surface forcings, and use the same method to combine results from the control and perturbation experiments to approximate the linear and non-linear behavior of those model variables.

## Acknowledgements

This study is supported by grants from the Natural Environment Research Council (NERC), including [1] The North Atlantic Climate System Integrated Study (ACSIS) (grant NE/N018028/1, author DJ), [2] Securing Multidisciplinary UndeRstanding and Prediction of Hiatus and

Surge events (SMURPHS) (grant NE/N006038/1, author EB), and [3] Ocean Regulation of Climate by Heat and Carbon Sequestration and Transports (ORCHESTRA, grant NE/N018095/1, authors EB, AM). The ECCOv4-r2 model setup used in this work is available for download on Github (https://github.com/gaelforget/ECCOv4) as an instance of the MIT general circulation model (MITgcm, http://mitgcm.org/). Numerical model runs were carried out on ARCHER, the UK national HPC facility (http://archer.ac.uk/). Adjoint code was generated using the TAF software tool, created and maintained by FastOpt GmbH (http://www.fastopt.com/).

## References

Adcroft, A., Campin, J.-M., Hill, C., & Marshall, J. (2004, dec). Implementation of an AtmosphereOcean General Circulation Model on the Expanded Spherical Cube. *Monthly Weather Review*, *132*(12), 2845–2863. Retrieved from http://journals.ametsoc.org/doi/abs/10.1175/MWR2823.1 doi: 10.1175/MWR2823.1

Bindoff, N. L., & Mcdougall, T. J. (1994). Diagnosing climate change and ocean ventilation using hydrographic data. *Journal of Physical Oceanography*, *24*(6), 1137–1152.

Cerovečki, I., Meijers, A. J., Mazloff, M. R., Gille, S. T., Tamsitt, V. M., & Holland, P. R. (2019). The effects of enhanced sea ice export from the Ross sea on recent cooling and freshening of the Southeast Pacific. *Journal of Climate*, *32*(7), 2013–2035.

Close, S. E., Naveira Garabato, A. C., McDonagh, E. L., King, B. A., Biuw, M., & Boehme, L. (2013). Control of Mode and Intermediate Water Mass Properties in Drake Passage by the Amundsen Sea Low. *Journal of Climate*, *26*(14), 5102-5123. Retrieved from https://doi.org/10.1175/JCLI-D-12-00346.1 doi: 10.1175/JCLI-D-12-00346.1

Forget, G., Campin, J.-M., Heimbach, P., Hill, C. N., Ponte, R. M., & Wunsch, C. (2015, oct). ECCO version 4: an integrated framework for non-linear inverse modeling and global ocean state estimation. *Geoscientific Model Development*, *8*(10), 3071–3104. Retrieved from http://www.geosci-model-dev.net/8/3071/2015/ doi: 10.5194/gmd-8-3071-2015

Forget, G., Ferreira, D., & Liang, X. (2015). On the observability of turbulent transport rates by Argo: Supporting evidence from an inversion experiment. *Ocean Science*, *11*(5), 839–853. doi: 10.5194/os-11-839-2015

Frölicher, T. L., Sarmiento, J. L., Paynter, D. J., Dunne, J. P., Krasting, J. P., & Winton, M. (2015, jan). Dominance of the Southern Ocean in Anthropogenic Carbon and Heat Uptake in CMIP5 Models. *Journal of Climate*, *28*(2), 862–886. Retrieved from http://journals.ametsoc.org/doi/10.1175/JCLI-D-14-00117.1 doi: 10.1175/JCLI-D-14-00117.1

Gao, L., Rintoul, S. R., & Yu, W. (2018, jan). Recent wind-driven change in Subantarctic Mode Water and its impact on ocean heat storage. *Nature Climate Change*, *8*(1), 58–63. Retrieved from http://dx.doi.org/10.1038/s41558-017-0022-8http://www.nature.com/articles/s41558-017-0022-8 doi: 10.1038/s41558-017-0022-8

Hanawa, K., & Talley, L. D. (2001). Chapter 5.4 Mode waters. In G. Siedler, J. Church, & J. Gould (Eds.), *Ocean circulation and climate* (Vol. 77, pp. 373–386). Academic Press. Retrieved from http://www.sciencedirect.com/science/article/pii/S0074614201801297 doi: https://doi.org/10.1016/S0074-6142(01)80129-7

Hyder, P. (2020).
*submitted*.

Iudicone, D., Rodgers, K. B., Schopp, R., & Madec, G. (2007, jan). An Exchange Window for the Injection of Antarctic Intermediate Water into the

South Pacific. *Journal of Physical Oceanography*, *37*(1), 31–49. Retrieved from http://journals.ametsoc.org/doi/abs/10.1175/JPO2985.1 doi: 10.1175/JPO2985.1

Jones, D. C., Boland, E., Meijers, A. J., Forget, G., Josey, S. A., Sallee, J., & Shuckburgh, E. (2019, dec). Heat Distribution in the Southeast Pacific Is Only Weakly Sensitive to High–Latitude Heat Flux and Wind Stress. *Journal of Geophysical Research: Oceans*, *124*(12), 8647–8666. Retrieved from https://onlinelibrary.wiley.com/doi/abs/10.1029/2019JC015460 doi: 10.1029/2019JC015460

Jones, D. C., Forget, G., Sinha, B., Josey, S. A., Boland, E. J. D., Meijers, A. J. S., & Shuckburgh, E. (2018, apr). Local and Remote Influences on the Heat Content of the Labrador Sea: An Adjoint Sensitivity Study. *Journal of Geophysical Research: Oceans*, *123*(4), 2646–2667. Retrieved from http://doi.wiley.com/10.1002/2018JC013774 doi: 10.1002/2018JC013774

Khatiwala, S., Tanhua, T., Mikaloff Fletcher, S., Gerber, M., Doney, S. C., Graven, H. D., ... Sabine, C. L. (2013, apr). Global ocean storage of anthropogenic carbon. *Biogeosciences*, *10*(4), 2169–2191. Retrieved from https://www.biogeosciences.net/10/2169/2013/ doi: 10.5194/bg-10-2169-2013

Landschützer, P., Gruber, N., Haumann, F. A., Rödenbeck, C., Bakker, D. C., Van Heuven, S., ... Wanninkhof, R. (2015, sep). The reinvigoration of the Southern Ocean carbon sink. *Science*, *349*(6253), 1221–1224. Retrieved from http://www.ncbi.nlm.nih.gov/pubmed/26359401 doi: 10.1126/science.aab2620

Le Quéré, C., Andrew, R. M., Friedlingstein, P., Sitch, S., Pongratz, J., Manning, A. C., ... Zhu, D. (2018, mar). Global Carbon Budget 2017. *Earth System Science Data*, *10*(1), 405–448. Retrieved from https://www.earth-syst-sci-data.net/10/405/2018/ doi: 10.5194/essd-10-405-2018

Levitus, S., Antonov, J. I., Boyer, T. P., Baranova, O. K., Garcia, H. E., Locarnini, R. A., ... Zweng, M. M. (2012, may). World ocean heat content and thermosteric sea level change (0-2000 m), 1955-2010. *Geophysical Research Letters*, *39*(10). Retrieved from http://doi.wiley.com/10.1029/2012GL051106 doi: 10.1029/2012GL051106

Lumpkin, R., & Speer, K. (2007, oct). Global Ocean Meridional Overturning. *Journal of Physical Oceanography*, *37*(10), 2550–2562. Retrieved from http://journals.ametsoc.org/doi/abs/10.1175/JPO3130.1 doi: 10.1175/JPO3130.1

Marotzke, J., Giering, R., Zhang, K. Q., Stammer, D., Hill, C., & Lee, T. (1999). Construction of the adjoint MIT ocean general circulation model and application to Atlantic heat transport sensitivity. *Journal of Geophysical Research*, *104547*(15), 529–29. doi: 10.1029/1999JC900236

Marshall, J., & Speer, K. (2012). Closure of the meridional overturning circulation through southern ocean upwelling. *Nature Geoscience*, *5*(3), 171.

McDougall, T. J., & Barker, P. M. (2011). Getting started with TEOS-10 and the Gibbs Seawater (GSW) oceanographic toolbox. *SCOR/IAPSO WG*, *127*, 1–28.

Meijers, A., Cerovečki, I., King, B., & Tamsitt, V. (2019). A see-saw in Pacific Subantarctic Mode Water formation driven by atmospheric modes. *Geophysical Research Letters*(46). doi: 10.1029/2019GL085280

Mikaloff Fletcher, S. E., Gruber, N., Jacobson, A. R., Doney, S. C., Dutkiewicz, S., Gerber, M., ... Sarmiento, J. L. (2006, jun). Inverse estimates of anthropogenic CO 2 uptake, transport, and storage by the ocean. *Global Biogeochemical Cycles*, *20*(2). Retrieved from http://doi.wiley.com/10.1029/2005GB002530 doi: 10.1029/2005GB002530

Naveira Garabato, A. C., Jullion, L., Stevens, D. P., Heywood, K. J., & King, B. A. (2009). Variability of Subantarctic Mode Water and Antarctic

Intermediate Water in the Drake Passage during the late-twentieth and early-twenty-first centuries. *Journal of Climate*, *22*(13), 3661–3688. doi: 10.1175/2009JCLI2621.1

Newman, L., Talley, L., Mazloff, M., Galton-Fenzi, B., Ackley, S., Heimbach, P., ... Sparrow, M. (2015). *Southern Ocean community comment on the Year of Polar Prediction Implementation Plan, SOOS Report Series* (Tech. Rep. No. 2). Retrieved from `http://www.soos.aq/`

Pillar, H. R., Heimbach, P., Johnson, H. L., & Marshall, D. P. (2016, may). Dynamical Attribution of Recent Variability in Atlantic Overturning. *Journal of Climate*, *29*(9), 3339–3352. doi: 10.1175/JCLI-D-15-0727.1

Rintoul, S. R., & England, M. H. (2002, may). Ekman Transport Dominates Local AirSea Fluxes in Driving Variability of Subantarctic Mode Water. *Journal of Physical Oceanography*, *32*(5), 1308–1321. Retrieved from `http://journals.ametsoc.org/doi/abs/10.1175/1520-0485{\%}282002{\%}29032{\%}3C1308{\%}3AETDLAS{\%}3E2.0.CO{\%}3B2` doi: 10.1175/1520-0485(2002)032⟨1308:ETDLAS⟩2.0.CO;2

Roemmich, D., Church, J., Gilson, J., Monselesan, D., Sutton, P., & Wijffels, S. (2015). Unabated planetary warming and its ocean structure since 2006. *Nature climate change*, *5*(3), 240.

Sloyan, B. M., Talley, L. D., Chereskin, T. K., Fine, R., Holte, J., Sloyan, B. M., ... Holte, J. (2010, jul). Antarctic Intermediate Water and Subantarctic Mode Water Formation in the Southeast Pacific: The Role of Turbulent Mixing. *Journal of Physical Oceanography*, *40*(7), 1558–1574. Retrieved from `http://journals.ametsoc.org/doi/abs/10.1175/2010JPO4114.1` doi: 10.1175/2010JPO4114.1

Song, H., Marshall, J., Follows, M. J., Dutkiewicz, S., & Forget, G. (2016, jun). Source waters for the highly productive Patagonian shelf in the southwestern Atlantic. *Journal of Marine Systems*, *158*, 120–128. doi: 10.1016/j.jmarsys.2016.02.009

Strobach, E., Molod, A., Forget, G., Campin, J. M., Hill, C., Menemenlis, D., & Heimbach, P. (2018, dec). Consequences of different air-sea feedbacks on ocean using MITgcm and MERRA-2 forcing: Implications for coupled data assimilation systems. *Ocean Modelling*, *132*, 91–111. doi: 10.1016/j.ocemod.2018.10.006

Verdy, A., Mazloff, M. R., Cornuelle, B. D., Kim, S. Y., Verdy, A., Mazloff, M. R., ... Kim, S. Y. (2014, jan). Wind-Driven Sea Level Variability on the California Coast: An Adjoint Sensitivity Analysis. *Journal of Physical Oceanography*, *44*(1), 297–318. Retrieved from `http://journals.ametsoc.org/doi/abs/10.1175/JPO-D-13-018.1` doi: 10.1175/JPO-D-13-018.1